Extreme Mechanics Letters 56 (2022) 101847

Contents lists available at ScienceDirect

Extreme Mechanics Letters

journal homepage: www.elsevier.com/locate/eml

Inverter-based elastic metamaterials for band gap at extremely low frequency

Faisal Jamil [a], Fei Chen [a], Bolei Deng [b,c], Robert G. Parker [a], Pai Wang [a,*]

[a] Department of Mechanical Engineering, University of Utah, Salt Lake City, UT 84112, USA
[b] Department of Electrical Engineering and Computer Science, Massachusetts Institute of Technology, Cambridge, MA 02139, USA
[c] Department of Mechanical Engineering, Massachusetts Institute of Technology, Cambridge, MA 02139, USA

ARTICLE INFO

Article history:
Received 3 June 2022
Received in revised form 12 July 2022
Accepted 19 July 2022
Available online 2 August 2022

Keywords:
Elastic metamaterials
Inerter
Ultra-low frequency
Band gap
Vibration mitigation

ABSTRACT

We reveal the unique and fundamental advantage of inerter-based elastic metamaterials by a comparative study among different configurations. When the embedded inerter is connected to the matrix material on both ends, the metamaterial shows definite superiority in forming a band gap in the ultra-low frequency - equivalently the ultra-long wavelength - regime, where the unit cell size can be four or more orders of magnitude smaller than the operating wavelength. In addition, our parametric studies in both one and two dimensions pave the way towards designing next-generation metamaterials for structural vibration mitigation.

Mitigation of low-frequency vibrations has long been a major challenge. One promising research direction points to architected materials — widely referred to as acoustic or elastic metamaterials [1–6]. They can exhibit a phononic band gap, i.e., a range of frequencies in which no vibration can propagate. While many recent studies attempted to demonstrate low-frequency band gaps [7–20,20–32], there is no consensus on which frequency ranges should be called "low" or "ultra-low". The exact meaning of low frequency varies from a fraction of one Hz [12,21], to several Hz [7,8,20], and up to many kHz [11,23,28]. The word "low" is a relative concept that depends on application-specific scenarios.

To facilitate a generally meaningful discussion and a fair comparison among different systems and configurations, here we focus on a universal and dimensionless frequency for all vibro-elastic metamaterials: $f = a/\lambda$, where a denotes the size of a metamaterial unit, and λ is the operating wavelength. All scattering-based band gaps in phononic crystals [33,34] are at the order of $f = a/\lambda \sim 1$. In contrast, locally resonant metamaterials embedded with mass-resonators [35,36] usually exhibit band gaps at a much lower frequency range of $f = a/\lambda \sim 10^{-2}$ to 10^{-3}.

In this Letter, we demonstrate the unique capability of inerter-based metamaterials in forming band gaps at the ultra-low dimensionless frequencies, where $f = a/\lambda \sim 10^{-4}$. The key component is the inerter, a two terminal mechanical device offering a *frequency-independent* inertia much larger than its own physical mass [37,38]. As illustrated in Fig. 1, this is possible because the inerter couples linear relative motions between its two ends to the rotation of a flywheel. The flywheel moment of inertia can be amplified to produce a large inertial effect. The use of rotational motion also makes it possible for the device to be compact. Like springs and dampers, the inerter is a passive device without the need of any active control. As shown in Fig. 1(a), the inerter's behavior is characterized by the response force, $F = b(\ddot{u}_1 - \ddot{u}_2)$, where $\ddot{u}_1$ and $\ddot{u}_2$ are the accelerations at the two terminals. The constant b is called the inertance, which has the same unit as mass. The performance attributes of inerters have been experimentally verified with ball-screw designs [37,39–44], rack-pinion designs [37,39,40,45], and hydraulic designs [46,47]. Their basic structures are shown in Figs. 1(b), 1(c) and 1(d), respectively. In particular, the hydraulic inerter design benefits from the small physical mass of nearly incompressible fluid that fills the inerter, so that it can produce an inertance that is 1.5×10^6 times larger than its own the physical mass [47].

While there have been several pioneering attempts to incorporate inerters into metamaterial designs [48–54]. A critical study to identify and overcome the fundamental hurdles is still missing. With theoretical and numerical analyses of different designs, we investigate the basic challenges and offer a road map to realize vibration-band-gap metamaterials with unit cells in the ultra-deep sub-wavelength scale of $a/\lambda \sim 10^{-4}$.

To start, we model any matrix material or base structure of metamaterials as a spring-mass chain with stiffness K and point

* Corresponding author.
E-mail address: pai.wang@utah.edu (P. Wang).

https://doi.org/10.1016/j.eml.2022.101847
2352-4316/

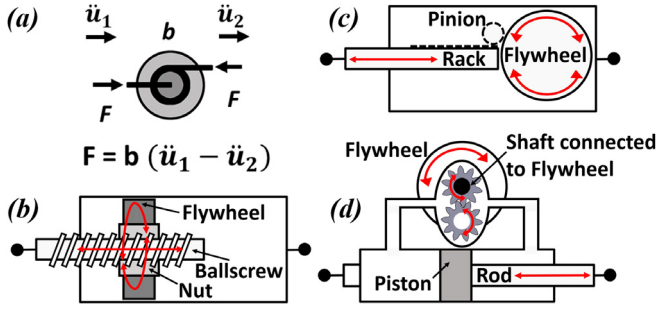

Fig. 1. Conceptual schematics of inerters: (a) Abstract symbol and force response. (b) Ball-screw inerter. (c) Rack-and-pinion inerter. (d) Hydraulic inerter.

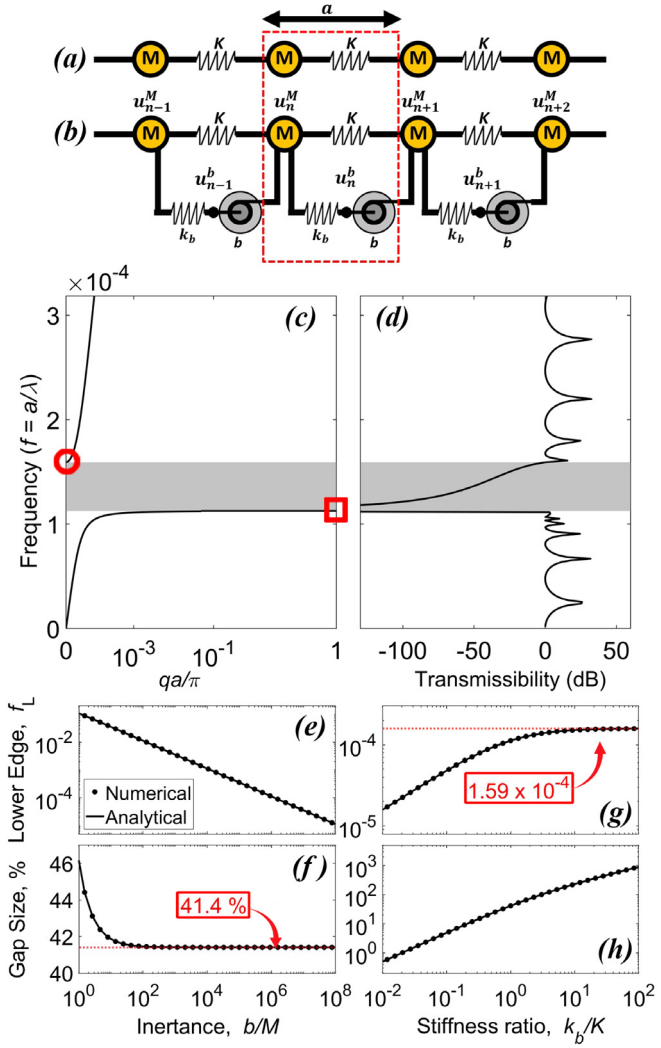

Fig. 2. Discrete models and band gaps: (a) Abstraction of any matrix material as a spring-mass chain; (b) Inerter-based metamaterial; (c) Dispersion curves and band gap (shaded region) of inerter-based metamaterial shown in (b) with $b/m_b = b/M = 10^6$ and $k_b/K = 1$; and (d) Finite-chain response of inerter-based metamaterial with 1000 unit cells. The transmissibility is calculated as the ratio between output and input amplitudes. Parametric studies on the band gap lower edge frequency and relative size: (e) and (f) show the effects of change in the inertance ratio, $\mu_b = b/M$, with fixed $\kappa_b = k_b/K = 1$. (g) and (h) show the effects of change in the stiffness ratio, $\kappa_b = k_b/K$, with fixed $\mu_b = b/M = 10^6$.

mass M, as shown in Fig. 2(a). This model is valid since we aim at the long-wavelength limit of $\lambda \gg a$, where the discrete nature of the main chain has negligible impact on the results. With this setup, we can normalize all metamaterial dispersion relations according to the main-chain wave speed in the long-wavelength limit, $c = a\sqrt{K/M}$, so that all band gap frequencies are non-dimensionalized [1,38] as $f = \omega a/(2\pi c) = a/\lambda$, where ω is the dimensional angular frequency in metamaterial dispersion relations.

We analyze three types of metamaterial designs with: embedded inerters [48,49,52,53], inerter-mass-resonators [48–52,54,55], and traditional mass-resonators [35,36], as shown in Figs. 2(b), 4(a) and 4(b), respectively. Applying the Bloch theorem [2,38], we calculate the dispersion relations of each system and investigate their behaviors at the low-frequency limit.

First, we consider metamaterials with the embedded inerter and no other additional mass, as illustrated in Fig. 2(b). The model has two degrees of freedom in the unit cell: u^M — displacement of mass M on the main chain and u^b — displacement of the point between stiffness k_b and inerter b on the side chain. With the parameters $k_b/K = 1$ and $b/M = 10^6$, the dispersion relation plotted in Fig. 2(c) shows a band gap as the grey-shaded range near $f = a/\lambda \sim 10^{-4}$. The horizontal axis of normalized wave number qa/π is shown in logarithmic scale because the band-gap effects happen at very long wavelength. This ultra-low frequency band gap is further demonstrated by transmission attenuation in the steady-state dynamics simulation of a finite chain [38], with results shown in Fig. 2(d). The band gap's lower edge frequency, f_L, is the eigen-frequency of the first band at $q = \pi/a$, as labelled by a red square in Fig. 2(c). Similarly, the band gap's upper edge frequency, f_U, is the eigen-frequency of the second band at $q = 0$, as labelled by a red circle in Fig. 2(c). As good non-dimensionalized measures for comparison purposes, we characterize the band gap by two quantities: (1) The starting dimensionless frequency, f_L; and (2) The relative gap size $\Delta f = (f_U - f_L)/f_L$. Fig. 2(e) shows the numerical results as $f_L = 1.125 \times 10^{-4}$ with a relative gap size of $\Delta f \approx 41.4\%$.

More generally, we can obtain the analytical equations,

$$f_L = \frac{1}{2\pi}\sqrt{\chi_b - \sqrt{\chi_b^2 - 4\frac{\kappa_b}{\mu_b}}} \quad \text{and} \quad f_U = \frac{1}{2\pi}\sqrt{\frac{\kappa_b}{\mu_b}}, \tag{1}$$

where $\chi_b = 2\kappa_b + \kappa_b/(2\mu_b) + 2$, $\kappa_b = k_b/K$, and $\mu_b = b/M$. These closed-form results enable us to perform asymptotic convergence analyses [38]. At the limit of large inertance, $\mu_b \gg \kappa_b$, we have

$$f_L \to \frac{1}{2\pi}\sqrt{\frac{\kappa_b}{\mu_b(\kappa_b+1)}} \quad \text{and} \quad \Delta f \to \sqrt{\kappa_b + 1} - 1. \tag{2}$$

These equations reveal a unique advantage of the design with embedded inerters: As the inertance $b = \mu_b M$ increases, the band gap shifts to a lower frequency. At the same time, the relative gap size, Δf, approaches a finite and low limit, keeping the band gap open at very low frequencies. This convergence is also shown together with numerical results in Figs. 2(e) and 2(f) with $\kappa_b = k_b/K = 1$, where the gap size converges to $\Delta f = \sqrt{2} - 1 \approx 41.4\%$ for large μ_b. In the same limit, we can also get the modal displacement ratios at the gap edges as:

$$\begin{aligned} U^b/U^M &\to 1 + 2/\kappa_b \quad \text{at} \quad f = f_L, \\ U^b/U^M &\to 1 \quad \text{at} \quad f = f_U, \end{aligned} \tag{3}$$

where U^b and U^M are modal amplitudes of u^b and u^M, respectively. Furthermore, taking the additional limit of $\kappa_b \gg 1$ gives

$$f_L \to \frac{1}{2\pi}\sqrt{\frac{1}{\mu_b}}, \quad \Delta f \to \sqrt{\kappa_b}, \tag{4}$$
$$U^b/U^M \to 1 \quad \text{at both } f_L \text{ and } f_U.$$

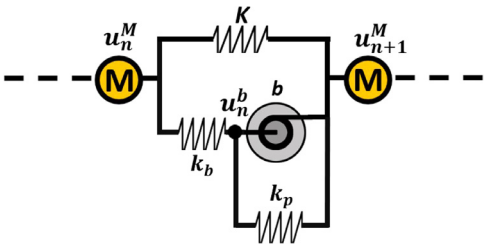

Fig. 3. The unit cell of Inerter-based metamaterial with an additional stiffness, k_p, parallel to the embedded inerter.

This shows that it is beneficial to have stiff connections between the inerter and the main chain: While we can get larger gap size as $k_b = \kappa_b K$ increases, the gap's starting frequency will saturate and converges to a finite limit, retaining the ultra-low frequency feature with large inertance. This high-stiffness convergence is shown together with numerical results in Figs. 2(g) and 2(h) with $\mu_b = b/M = 10^6$. The lower gap edge converges to $f_L = 10^{-3}/(2\pi) \approx 1.59 \times 10^{-4}$.

An important variant design involves an additional stiffness, k_p, parallel to the embedded inerter. As shown in Fig. 3, each unit cell still has two degrees of freedom. We perform the same analyses as before and obtain the equations for both upper and lower edges of the band gap in this case as

$$f_L = \frac{1}{2\pi}\sqrt{\chi_p - \sqrt{\chi_p^2 - \frac{4(\kappa_b + \kappa_b\kappa_p + \kappa_p)}{\mu_b}}}, \tag{5a}$$

$$f_U = \frac{1}{2\pi}\sqrt{\frac{(\kappa_b + \kappa_p)}{\mu_b}}, \tag{5b}$$

where $\chi_p = 2\kappa_b + (\kappa_b + \kappa_p)/(2\mu_b) + 2$, $\kappa_b = k_b/K$, $\kappa_p = k_p/K$, and $\mu_b = b/M$. At the limit of large inertance ($\mu_b \gg \kappa_b, \kappa_p$) and taking $\kappa_b = 1$, we get the asymptotic convergence

$$f_L \to \frac{1}{2\pi}\sqrt{\frac{2\kappa_p + 1}{2\mu_b}} \quad \text{and} \quad \Delta f \to \sqrt{1 + \frac{1}{2\kappa_p + 1}} - 1, \tag{6}$$

which indicate that, as the parallel stiffness k_p increases, not only does f_L get higher, but Δf also gets smaller. Hence, the parallel stiffness k_p has only detrimental effects, and it is best to set k_p to zero to achieve both design objectives of lower gap frequency and larger gap size.

Therefore, the optimal design requires that the inerter has very large inertance and very stiff connections with the base structure, and it is better *not* to incorporate any stiffness parallel to the inerter. Because it is possible to fabricate inerters with inertance more than a million times of its actual mass ($\mu_b \sim 10^6$) [47], the embedded inerter design shown in Fig. 2(b) is practical for engineering applications.

Next, we study an alternative metamaterial design with embedded mass-inerter resonators, as illustrated in Fig. 4(a). One end of the inerter is connected to the main chain, while the other end is connected to a resonator mass m. This results in a model with three degrees of freedom in each unit cell: u^M – displacement of mass M on the main chain, u^b – displacement of the point between stiffness k_b and inerter b, and u^m - displacement of the resonator mass m. Applying the same Bloch-wave procedures as before yields the dispersion bands for this system [38]. At the limit of large inertance ($\mu_b \gg \mu_m, \kappa_b, \kappa_f$) and low frequency ($f \ll 1$), we arrive at

$$f_L \to \frac{1}{2\pi}\sqrt{\frac{\kappa_b\kappa_m}{\mu_b(\kappa_b + \kappa_m)}} \quad \text{and} \quad \Delta f \to 0, \tag{7}$$

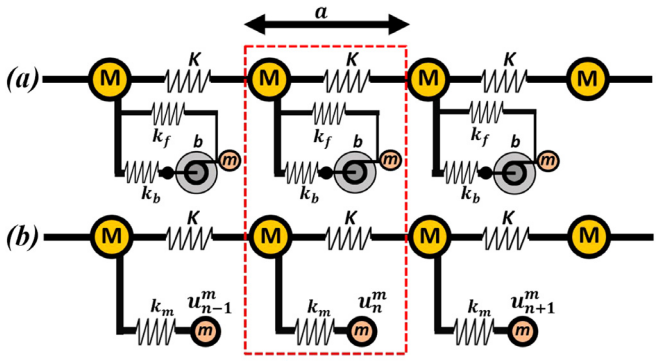

Fig. 4. Discrete models: (a) Metamaterial with inerter-mass-resonators; (b) Metamaterial with mass-resonators;.

where $\mu_b = b/M$, $\mu_m = m/M$, $\kappa_b = k_b/K$, and $\kappa_f = k_f/K$. Since increasing the inertance closes the band gap ($\Delta f \to 0$), this mass-inerter-resonator design shown in Fig. 4(a) is not suitable to achieve ultra-low frequency band gaps.

Lastly, we also look into the traditional locally resonant metamaterials with embedded mass-resonators, as illustrated in Fig. 4 (b). The discrete model has two degrees of freedom in each unit cell: u^M – displacement of mass M on the main chain, and u^m – displacement of the resonator mass m. The analytical closed-form expressions of the band gap edges are [38,56]

$$f_L = \frac{1}{2\pi}\sqrt{\chi_m - \sqrt{\chi_m^2 - 4\frac{\kappa_m}{\mu_m}}}, \tag{8a}$$

$$f_U = \frac{1}{2\pi}\sqrt{\frac{\kappa_m}{\mu_m} + \kappa_m}, \tag{8b}$$

where $\chi_m = \kappa_m/2 + \kappa_m/(2\mu_m) + 2$, $\kappa_m = k_m/K$, and $\mu_m = m/M$. Based on Eq. (8a), in order to achieve ultra-low-frequency band gaps with $f_L \sim 10^{-4}$, we need $\mu_m/\kappa_m \sim 10^8$. On the other hand, we need to avoid the case of $\mu_m = m/M \gg 1$ since it would make the embedded mass-resonator too heavy as compared to the matrix material or base structure, and hence would be infeasible in most applications. The only viable choice is to adopt the ultra-low-stiffness design with $\mu_m \sim 1$ and $\kappa_m \ll 1$, at which limit we get:

$$f_L \to \frac{1}{2\pi}\sqrt{\frac{\kappa_m}{\mu_m}} \quad \text{and} \quad \Delta f \to \sqrt{\mu_m + 1} - 1. \tag{9}$$

This approach to form a band gap at ultra-low frequencies may initially seem possible. In fact, with $\mu_m = m/M = 1$ and $\kappa_m = k_m/K = 5 \times 10^{-7}$, we obtain exactly the same dispersion bands as those plotted in Fig. 2(c). However, in the same limit of $\mu_m \sim 1$ and $\kappa_m \ll 1$, we get the modal displacement ratios at the gap edges as

$$\begin{aligned} U^b/U^M &\to 4/\kappa_m \quad \text{at} \quad f = f_L, \\ U^b/U^M &\to 1/\mu_m \quad \text{at} \quad f = f_U. \end{aligned} \tag{10}$$

Hence, the same design parameters give rise to a very high modal displacement ratio, $U^m/U^M \to 4/\kappa_m = 8 \times 10^6$ at the lower gap edge f_L (marked with red square in Fig. 2(c)). This means the resonator mass would vibrate with an amplitude that is millions of times of the vibration amplitude in the main chain. Therefore, the ultra-low stiffness design here is impractical in most application scenarios.

Based on the analyses of all three designs above, we conclude that the inerter-based metamaterial design depicted in Fig. 2(b) is the only suitable solution to achieve band gaps at the ultra-low dimensionless frequency of $f = a/\lambda \sim 10^{-4}$ or lower.

To further demonstrate the efficacy and practicality of this design, we perform numerical studies on two-dimensional lattices with embedded inerters. Due to the close relevance to engineering applications, there have been many pioneering studies realizing band gaps in two- and three-dimensional metamaterials with other lever- or geometry-based inertial amplified structures [57–60], as well as two-dimensional structures that incorporate a flat plate [61–64] or a beam [50,53,65–69] as the base structure with inerter-based resonators. However, none of the designs so far can achieve band gaps at the ultra-low dimensionless frequency of $f = a/\lambda \sim 10^{-4}$. In the following, we investigate the viable design illustrated in Fig. 2(b) in two-dimensional systems.

Here, we show conceptual two-dimensional designs in the form of inerter-in-lattice configurations that can represent various engineering structures. As shown in Fig. 5(a), for graphic compactness, we use a blue straight line to represent a connection with main-chain stiffness K, side-chain stiffness k_b, and side-chain inertance b. We assume the displacement u^b at the point between stiffness k_b and inerter b is always rigidly constrained in the lateral direction of the connection unit, so that u_b is always along the direction of the connection. Then, we construct square (Fig. 5(b)) and triangular (Fig. 5(c)) lattices with this basic connection building block. All connections possess an embedded inerter on the side chain. Specifically for the square lattice, the diagonal connections are necessary to make the lattice statically stable, so that no zero-frequency band can exist. The crossing point of the two diagonal connections at the center of each square is not a joint, and there is no interactions here between the two diagonal connections. Although the formulations and derivations [38] are more challenging than those for one-dimensional cases, we can still study the two-dimensional designs via numerical results. With stiffness ratio $\kappa_b = kb/K = 1$ and inertance ratio $\mu_b = b/M = 10^6$, we plot the dispersion curves of square and triangular lattices with embedded inerters in Figs. 5(d) and 5(e), respectively. A band gap exists in both cases with the lower gap edge frequency of $f_L = 1.125 \times 10^{-4}$ and the relative gap size of $\Delta f \approx 41.4\%$. Not only do the band gaps match each other in the two different lattices, but they also match the band gap of the one-dimensional configuration shown in Fig. 2(b). It might be counter-intuitive to have such close resemblance of dispersion relations for different lattices. The fundamental reason is that the effect happens in the very long wavelength limit of $\lambda \gg a$. In this regime, the wave only "sees" and "feels" the homogenized properties of the lattice geometry, and the unit-cell level structures and small length-scale details have minimal influence on the metamaterial behavior. As a result, the difference in lattice configurations has negligible impact on the ultra-low-frequency band gap.

To conclude, our analytical and numerical analyses offer clear guidelines to design elastic metamaterials with an ultra-low-frequency band gap: Each unit cell needs an embedded inerter with both terminals connected to the base material; no additional resonator mass should be used; to achieve band gaps at lower frequency, higher inertance is needed; and, to achieve wider band gaps, stiffer connection between the inerter and the base material is needed. These insights provide actionable guidelines for future studies towards low-frequency vibration mitigation using metamaterials. Furthermore, for future studies on experimental fabrications of inerter-based metamaterials, we anticipate two potential challenges: (1) Achieving high inertance-to-mass ratio, $\mu = b/m_b$ in a compact design; and (2) Optimizing motion transmission mechanisms between matrix material and inerters. Lastly, although this study is focused on periodic metamaterials, our analyses can be extended to quasi-crystalline [70–72], hyper-uniform [73–75], amorphous [76] or other non-periodic inerter-based metamaterial designs.

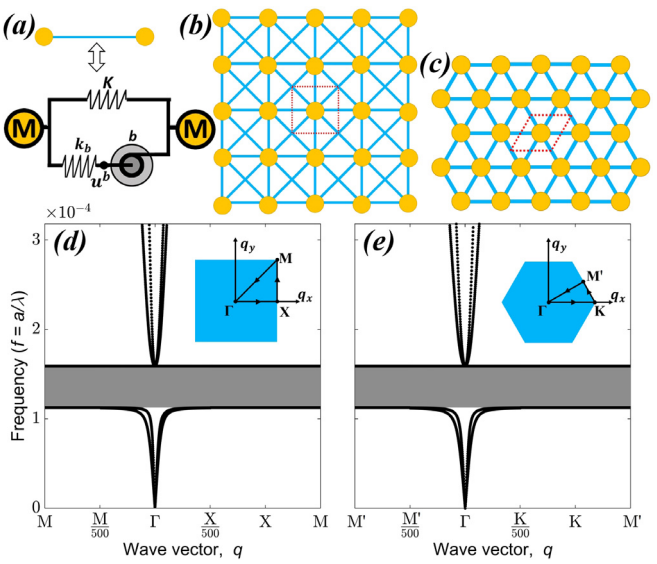

Fig. 5. Two-dimensional lattices with embedded inerters: (a) Basic connection unit used in both lattices. Note that u_b here is always just a single degree of freedom in any two-dimensional lattice, as we constrain it to allow displacement parallel to the connection only. (b) and (c) depict the square and triangular lattices with embedded inerters, respectively. With $\kappa_b = k_b/K = 1$ and $\mu_b = b/M = 10^6$, (d) and (e) show the dispersion bands of configurations (b) and (c), respectively. The blue insets of (d) and (e) illustrate Brillouin zones for square and triangular lattices, respectively. $\Gamma = (0, 0)$, X $= (1, 0)\pi/a$, M $= (0, 1)\pi/a$, K $= (4/3, 0)\pi/a$, and M' $= (1, 1/\sqrt{3})\pi/a$ are high-symmetry points at the boundaries of irreducible Brillouin zones.

Declaration of competing interest

The authors declare that they have no known competing financial interests or personal relationships that could have appeared to influence the work reported in this paper.

Data availability

All data and computational program code are shared as the Supporting Information (SI)

Acknowledgments

Both R.G.P and P.W. acknowledge the start-up research funds of the Department of Mechanical Engineering at University of Utah, USA. The support and resources from the Center for High Performance Computing at the University of Utah are gratefully acknowledged. The authors thank Prof. Peter Zhu, Dr. Xiaolong Tong, Sharat Paul and Md Nahid Hasan for inspirational discussions.

Appendix A. Supplementary data

Supplementary material related to this article can be found online at https://doi.org/10.1016/j.eml.2022.101847.

References

[1] M. Maldovan, E.L. Thomas, Periodic Materials and Interference Lithography: for Photonics, Phononics and Mechanics, John Wiley & Sons, 2009.
[2] M.I. Hussein, M.J. Leamy, M. Ruzzene, Dynamics of phononic materials and structures: Historical origins, recent progress, and future outlook, Appl. Mech. Rev. 66 (4) (2014).
[3] D. Mu, H. Shu, L. Zhao, S. An, A review of research on seismic metamaterials, Adv. Energy Mater. 22 (4) (2020) 1901148.

[4] L. Liu, H.P. Lee, A review: Elastic metamaterials and inverse design methods for shock and vibration mitigation, Int. J. Appl. Mech. 13 (09) (2021) 2150102.
[5] J. Ji, Q. Luo, K. Ye, Vibration control based metamaterials and origami structures: A state-of-the-art review, Mech. Syst. Signal Process. 161 (2021) 107945.
[6] H. Laghfiri, N. Lamdouar, Periodic structures as a countermeasure of traffic vibration and earthquake: A review, in: R. Saidi, B. El Bhiri, Y. Maleh, A. Mosallam, M. Essaaidi (Eds.), Advanced Technologies for Humanity, Springer International Publishing, Cham, 2022, pp. 359–373.
[7] S. Krodel, N. Thomé, C. Daraio, Wide band-gap seismic metastructures, Extreme Mech. Lett. 4 (2015) 111–117, http://dx.doi.org/10.1016/j.eml.2015.05.004.
[8] Y. Achaoui, B. Ungureanu, S. Enoch, S. Brûlé, S. Guenneau, Seismic waves damping with arrays of inertial resonators, Extreme Mech. Lett. 8 (2016) 30–37, http://dx.doi.org/10.1016/j.eml.2016.02.004.
[9] J.H. Oh, S. Qi, Y.Y. Kim, B. Assouar, Elastic metamaterial insulator for broadband low-frequency flexural vibration shielding, Phys. Rev. A 8 (5) (2017) 054034, http://dx.doi.org/10.1103/PhysRevApplied.8.054034.
[10] X. Fang, J. Wen, B. Bonello, J. Yin, D. Yu, Ultra-low and ultra-broadband nonlinear acoustic metamaterials, Nature Commun. 8 (1) (2017) http://dx.doi.org/10.1038/s41467-017-00671-9.
[11] A.O. Krushynska, A. Amendola, F. Bosia, C. Daraio, N.M. Pugno, F. Fraternali, Accordion-like metamaterials with tunable ultra-wide low-frequency band gaps, New J. Phys. 20 (7) (2018) 073051, http://dx.doi.org/10.1088/1367-2630/aad354.
[12] Muhammad, C. Lim, J. Reddy, Built-up structural steel sections as seismic metamaterials for surface wave attenuation with low frequency wide bandgap in layered soil medium, Eng. Struct. 188 (2019) 440–451, http://dx.doi.org/10.1016/j.engstruct.2019.03.046.
[13] Y. Chen, F. Qian, F. Scarpa, L. Zuo, X. Zhuang, Harnessing multi-layered soil to design seismic metamaterials with ultralow frequency band gaps, Mater. Des. 175 (2019) 107813, http://dx.doi.org/10.1016/j.matdes.2019.107813.
[14] L. D'Alessandro, R. Ardito, F. Braghin, A. Corigliano, Low frequency 3D ultra-wide vibration attenuation via elastic metamaterial, Sci. Rep. 9 (1) (2019) http://dx.doi.org/10.1038/s41598-019-44507-6.
[15] P. Sun, Z. Zhang, H. Guo, N. Liu, Y. Wang, Hierarchical square honeycomb metamaterials with low-frequency broad bandgaps and flat energy bands characteristics, J. Appl. Phys. 128 (23) (2020) 235102, http://dx.doi.org/10.1063/5.0056179.
[16] Y. Zeng, P. Peng, Q.-J. Du, Y.-S. Wang, B. Assouar, Subwavelength seismic metamaterial with an ultra-low frequency bandgap, J. Appl. Phys. 128 (1) (2020) 014901, http://dx.doi.org/10.1063/1.5144177.
[17] Y. Ruan, X. Liang, X. Hua, C. Zhang, H. Xia, C. Li, Isolating low-frequency vibration from power systems on a ship using spiral phononic crystals, Ocean Eng. 225 (2021) 108804, http://dx.doi.org/10.1016/j.oceaneng.2021.108804.
[18] D. Chen, H. Zi, Y. Li, X. Li, Low frequency ship vibration isolation using the band gap concept of sandwich plate-type elastic metastructures, Ocean Eng. 235 (2021) 109460, http://dx.doi.org/10.1016/j.oceaneng.2021.109460.
[19] Q. Lin, J. Zhou, H. Pan, D. Xu, G. Wen, Numerical and experimental investigations on tunable low-frequency locally resonant metamaterials, Acta Mech. Solida Sin. 34 (5) (2021) 612–623, http://dx.doi.org/10.1007/s10338-021-00220-4.
[20] M. Zhang, J. Yang, R. Zhu, Origami-based bistable metastructures for low-frequency vibration control, J. Appl. Mech. 88 (5) (2021) http://dx.doi.org/10.1115/1.4049953.
[21] Y. Huang, X. Zhang, Pentamode metamaterials with ultra-low-frequency single-mode band gap based on constituent materials, J. Phys.: Condens. Matter 33 (18) (2021) 185703, http://dx.doi.org/10.1088/1361-648X/abeebd.
[22] X. Wang, S. Wan, Y. Nian, P. Zhou, Y. Zhu, Periodic in-filled pipes embedded in semi-infinite space as seismic metamaterials for filtering ultra-low-frequency surface waves, Constr. Build. Mater. 313 (2021) 125498, http://dx.doi.org/10.1016/j.conbuildmat.2021.125498.
[23] Muhammad, C.W. Lim, Phononic metastructures with ultrawide low frequency three-dimensional bandgaps as broadband low frequency filter, Sci. Rep. 11 (1) (2021) http://dx.doi.org/10.1038/s41598-021-86520-8.
[24] W. Jiang, M. Yin, Q. Liao, L. Xie, G. Yin, Three-dimensional single-phase elastic metamaterial for low-frequency and broadband vibration mitigation, Int. J. Mech. Sci. 190 (2021) 106023, http://dx.doi.org/10.1016/j.ijmecsci.2020.106023.
[25] H.-F. Zhu, X.-W. Sun, T. Song, X.-D. Wen, X.-X. Liu, J.-S. Feng, Z.-J. Liu, Tunable characteristics of low-frequency bandgaps in two-dimensional multivibrator phononic crystal plates under prestrain, Sci. Rep. 11 (1) (2021) http://dx.doi.org/10.1038/s41598-021-87904-6.
[26] M.H. Bae, W. Choi, J.M. Ha, M. Kim, H.M. Seung, Extremely low frequency wave localization via elastic foundation induced metamaterial with a spiral cavity, Sci. Rep. 12 (1) (2022) http://dx.doi.org/10.1038/s41598-022-08002-9.
[27] Q. Li, M. Zhang, Elastic metamaterials of hexagonal unit cells with double-cone arms from pentamode to band gap at low frequencies, Crystals 12 (5) (2022) http://dx.doi.org/10.3390/cryst12050604.
[28] N.H. Vo, T.M. Pham, H. Hao, K. Bi, W. Chen, A reinvestigation of the spring-mass model for metamaterial bandgap prediction, Int. J. Mech. Sci. 221 (2022) 107219.
[29] H. Zi, Y. Li, Low-frequency broadband vibration attenuation of sandwich plate-type metastructures with periodic thin-wall tube cores, J. Low Freq. Noise Vib. Act. Control 41 (1) (2022) 330–339.
[30] Q. Lin, J. Zhou, K. Wang, D. Xu, G. Wen, Q. Wang, C. Cai, Low-frequency locally resonant band gap of the two-dimensional quasi-zero-stiffness metamaterials, Int. J. Mech. Sci. (2022) 107230.
[31] Y. Zeng, L. Cao, S. Wan, T. Guo, Y.-F. Wang, Q.-J. Du, B. Assouar, Y.-S. Wang, Seismic metamaterials: Generating low-frequency bandgaps induced by inertial amplification, Int. J. Mech. Sci. 221 (2022) 107224.
[32] Z. Yan, H. Xiao, Y. Liu, T. Tan, Band-gap dynamics and programming for low-frequency broadband elastic metamaterial, Compos. Struct. (2022) 115535.
[33] M.M. Sigalas, Elastic and acoustic wave band structure, J. Sound Vib. 158 (2) (1992) 377–382.
[34] M.S. Kushwaha, P. Halevi, L. Dobrzynski, B. Djafari-Rouhani, Acoustic band structure of periodic elastic composites, Phys. Rev. Lett. 71 (13) (1993) 2022.
[35] Z. Liu, X. Zhang, Y. Mao, Y. Zhu, Z. Yang, C.T. Chan, P. Sheng, Locally resonant sonic materials, Science 289 (5485) (2000) 1734–1736.
[36] P. Wang, F. Casadei, S. Shan, J.C. Weaver, K. Bertoldi, Harnessing buckling to design tunable locally resonant acoustic metamaterials, Phys. Rev. Lett. 113 (1) (2014) 014301.
[37] M.Z. Chen, C. Papageorgiou, F. Scheibe, F.-C. Wang, M.C. Smith, The missing mechanical circuit element, IEEE Circuits Syst. Mag. 9 (1) (2009) 10–26.
[38] See Supplemental Information at URL for additional results, detailed derivations, and calculation procedures. The Supplemental Information cites Refs. [1, 2, 36, 37, 39-47, 56, 77-84].
[39] C. Papageorgiou, M.C. Smith, Laboratory experimental testing of inerters, in: Proceedings of the 44th IEEE Conference on Decision and Control, IEEE, 2005, pp. 3351–3356.
[40] C. Papageorgiou, N.E. Houghton, M.C. Smith, Experimental testing and analysis of inerter devices, J. Dyn. Syst. Meas. Control 131 (1) (2009).
[41] Y. Shen, L. Chen, X. Yang, D. Shi, J. Yang, Improved design of dynamic vibration absorber by using the inerter and its application in vehicle suspension, J. Sound Vib. 361 (2016) 148–158.
[42] X. Sun, L. Chen, S. Wang, X. Zhang, X. Yang, Performance investigation of vehicle suspension system with nonlinear ball-screw inerter, Int. J. Automot. Technol. 17 (3) (2016) 399–408.
[43] L. Yuehao, C. Zhe, H. Niaoqing, Y. Yi, X. Zhuo, Modeling, design and experiments of a ball-screw inerter with mechanical diodes, J. Sound Vib. 504 (2021) 116121.
[44] L. Yuehao, C. Zhe, H. Niaoqing, Y. Yi, Y. Zhengyang, Study of dynamic breakdown of inerter and the improved design, Mech. Syst. Signal Process. 167 (2022) 108520.
[45] R. Wang, X. Meng, D. Shi, X. Zhang, Y. Chen, L. Chen, Design and test of vehicle suspension system with inerters, Proc. Inst. Mech. Eng. C 228 (15) (2014) 2684–2689.
[46] F.-C. Wang, M.-F. Hong, T.-C. Lin, Designing and testing a hydraulic inerter, Proc. Inst. Mech. Eng. C 225 (1) (2011) 66–72.
[47] S. Nakaminami, H. Kida, K. Ikago, N. Inoue, Dynamic testing of a full-scale hydraulic inerter-damper for the seismic protection of civil structures, in: 7th International Conference on Advances in Experimental Structural Engineering, AESE 2017, Eucentre, 2017, pp. 41–54.
[48] P.P. Kulkarni, J.M. Manimala, Longitudinal elastic wave propagation characteristics of inertant acoustic metamaterials, J. Appl. Phys. 119 (24) (2016) 245101.
[49] H. Al Ba'ba'a, D. DePauw, T. Singh, M. Nouh, Dispersion transitions and pole-zero characteristics of finite inertially amplified acoustic metamaterials, J. Appl. Phys. 123 (10) (2018) 105106.
[50] X. Fang, K.-C. Chuang, X. Jin, Z. Huang, Band-gap properties of elastic metamaterials with inerter-based dynamic vibration absorbers, J. Appl. Mech. 85 (7) (2018) 071010.
[51] K. Madhamshetty, J.M. Manimala, Extraordinary wave manipulation characteristics of nonlinear inertant acoustic metamaterials, J. Franklin Inst. B 356 (14) (2019) 7731–7753.
[52] F. Sun, L. Xiao, Bandgap characteristics and seismic applications of inerter-in-lattice metamaterials, J. Eng. Mech. 145 (9) (2019) 04019067.
[53] M. Cajić, J. Christensen, S. Adhikari, Tuning of topological interface modes in an elastic beam array system with inerters, Int. J. Mech. Sci. 205 (2021) 106573.
[54] Y. Liu, J. Yang, X. Yi, D. Chronopoulos, Enhanced suppression of low-frequency vibration transmission in metamaterials with linear and nonlinear inerters, J. Appl. Phys. 131 (10) (2022) 105103.

[55] M. Wang, F.-F. Sun, S. Nagarajaiah, Y.-W. Li, Frequency-dependency/independency analysis of damping magnification effect provided by tuned inerter absorber and negative stiffness amplifying damper considering soil-structure interaction, Mech. Syst. Signal Process. 172 (2022) 108965.
[56] H. Al Ba'ba'a, M. Nouh, T. Singh, Formation of local resonance band gaps in finite acoustic metamaterials: A closed-form transfer function model, J. Sound Vib. 410 (2017) 429–446.
[57] G. Acar, C. Yilmaz, Experimental and numerical evidence for the existence of wide and deep phononic gaps induced by inertial amplification in two-dimensional solid structures, J. Sound Vib. 332 (24) (2013) 6389–6404.
[58] S. Taniker, C. Yilmaz, Design, analysis and experimental investigation of three-dimensional structures with inertial amplification induced vibration stop bands, Int. J. Solids Struct. 72 (2015) 88–97.
[59] R. Zaccherini, A. Colombi, A. Palermo, H.R. Thomsen, E.N. Chatzi, Stress-optimized inertial amplified metastructure with opposite chirality for vibration attenuation, 2021, arXiv preprint arXiv:2111.08594.
[60] R. Zaccherini, Granular metasurfaces and inertial amplified metastructures for vibration attenuation, (Ph.D. thesis), ETH Zurich, 2021.
[61] A.F. Russillo, G. Failla, G. Alotta, Ultra-wide low-frequency band gap in locally-resonant plates with tunable inerter-based resonators, Appl. Math. Model. 106 (2022) 682–695.
[62] T. Wang, Tunable band gaps in an inertant metamaterial plate with two-degree-of-freedom local resonance, Phys. Lett. A 384 (21) (2020) 126420.
[63] J. Li, P. Yang, S. Li, Reduction of sound transmission through finite clamped metamaterial-based double-wall sandwich plates with poroelastic cores, Acta Acust. United Acust. 105 (5) (2019) 850–868.
[64] T. Wang, J. Liu, M. Chen, Sound transmission loss of an inertant metamaterial plate submerged in moving fluids, Appl. Math. Model. (2022).
[65] X. Fang, K.-C. Chuang, X.-L. Jin, D.-F. Wang, Z.-L. Huang, An inertant elastic metamaterial plate with extra wide low-frequency flexural band gaps, J. Appl. Mech. 88 (2) (2021).
[66] Z. Dong, D. Chronopoulos, J. Yang, Enhancement of wave damping for metamaterial beam structures with embedded inerter-based configurations, Appl. Acoust. 178 (2021) 108013.
[67] L. Zhou, W. Han, S. Wan, Low frequency band gap for box girder attached IDVAs, Thin-Walled Struct. 174 (2022) 109088.
[68] Z. Dong, J. Yang, C. Zhu, D. Chronopoulos, T. Li, Energy flow and performance evaluation of inerter-based vibration isolators mounted on finite and infinite flexible foundation structures, Adv. Mech. Eng. 14 (1) (2022) 16878140211070461.
[69] A. Aladwani, A. Mohammed, M. Nouh, Tunable dissipation in elastic metamaterials via methodic reconfiguration of inertant mechanical networks, Meccanica (2022) 1–16.
[70] M.I.N. Rosa, Y. Guo, M. Ruzzene, Exploring topology of 1D quasiperiodic metastructures through modulated LEGO resonators, Appl. Phys. Lett. 118 (13) (2021) 131901, http://dx.doi.org/10.1063/5.0042294.
[71] R.L. Thomes, J.A. Mosquera-Sánchez, C.D. Marqui, Bandgap widening by optimized disorder in one-dimensional locally resonant piezoelectric metamaterials, J. Sound Vib. 512 (2021) 116369, http://dx.doi.org/10.1016/j.jsv.2021.116369.
[72] Y. Liu, L.F. Santos, E. Prodan, Topological gaps in quasiperiodic spin chains: A numerical and K-theoretic analysis, Phys. Rev. B 105 (3) (2022) 035115, http://dx.doi.org/10.1103/PhysRevB.105.035115.
[73] G. Gkantzounis, T. Amoah, M. Florescu, Hyperuniform disordered phononic structures, Phys. Rev. B 95 (9) (2017) 094120, http://dx.doi.org/10.1103/PhysRevB.95.094120.
[74] V. Romero-García, E. Chéron, S. Kuznetsova, J.-P. Groby, S. Félix, V. Pagneux, L.M. Garcia-Raffi, Wave transport in 1D stealthy hyperuniform phononic materials made of non-resonant and resonant scatterers, APL Mater. 9 (10) (2021) 101101, http://dx.doi.org/10.1063/5.0059928.
[75] S.M. Kuznetsova, J.-P. Groby, L.M. García-Raffi, V. Romero-García, Localized interface modes in one-dimensional hyperuniform acoustic materials, J. Phys. D: Appl. Phys. 54 (31) (2021) 315303, http://dx.doi.org/10.1088/1361-6463/ac006d.
[76] N.P. Mitchell, L.M. Nash, D. Hexner, A.M. Turner, W. Irvine, Amorphous topological insulators constructed from random point sets, Nat. Phys. 14 (4) (2018) 380–385.

Supporting Information for *Inerter-based Elastic Metamaterials for Band Gap at Extremely Low Frequency*

Faisal Jamil, Department of Mechanical Engineering, University of Utah, Salt Lake City, UT, USA.

Fei Chen, Department of Mechanical Engineering, University of Utah, Salt Lake City, UT, USA.

Bolei Deng, Computer Science and Artificial Intelligence Laboratory, Department of Electrical Engineering and Computer Science, and Department of Mechanical Engineering, Massachusetts Institute of Technology, Cambridge, MA, USA.

Robert G. Parker, Department of Mechanical Engineering, University of Utah, Salt Lake City, UT, USA.

Pai Wang, Department of Mechanical Engineering, University of Utah, Salt Lake City, UT, USA, pai.wang@utah.edu

Contents

S1 Inerter Designs

Conventional passive vibration mitigation systems include masses, springs and dampers. Both springs and dampers are two-terminal mechanical elements. Their force responses are related to the relative displacement and velocity of the two ends, respectively (Fig. S1(a) and (b)). In contrast, a mass is a single-terminal mechanical element, in which the relative motion of its two opposite sides does not contribute to the inertial effect. To mitigate low-frequency vibration, larger mass is usually necessary to provide enough inertia. However, increasing mass is not desirable as it makes the system heavy and bulky, and even not feasible for some cases where lightweight compact systems are essential. An inerter provides a much bigger inertial effect than its actual physical mass. Thus, it could be a promising candidate for mitigating low-frequency vibrations. As shown in Fig. S1(c), inerter[12, 14] is a two-terminal element that offers inertial effects. Its force response is proportional to the relative acceleration between the two terminals. The proportionality coefficient, b, of an inerter is called inertance and has the unit of mass.

The commonly manufactured inerters are: ballscrew [10, 3, 11, 13, 16, 21, 22], rack-and-pinion [10, 3, 11, 19] and hydraulic [17, 8] inerters. Fig. S1(d) and (e) show ball-screw and rack-pinion inerters, respectively. Here, the inertance depends predominantly on the size of the flywheel. Therefore, inertance produced by the inerters is limited by the physical size of

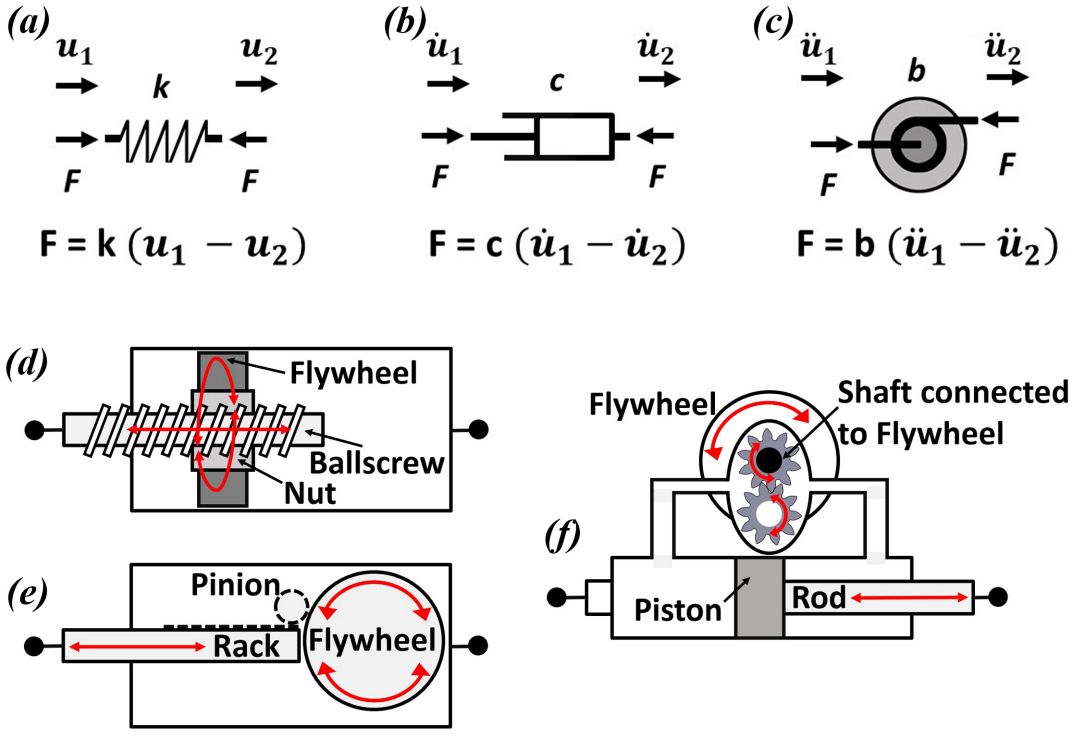

Figure S1: Two-terminal mechanical elements: (a) spring, (b) damper and (c) inerter. Mechanism illustration of a ball-screw inerter (d); rack-and-pinion inerter (e); and hydraulic inerter (f). u: displacement, $\dot{u}$: velocity, $\ddot{u}$: acceleration, F: force, k: stiffness, c: damping, and b: inertance.

the inerter. Fig. S1(f) shows hydraulic inerter that can produce very high inertance due to the inertial resistive force from the small amount of fluid filling up the inside of the inerter. A small V_m/A_p ratio can produce inertance of up to 1.5×10^6 times larger than the physical mass of the inerter, where V_m is the volume of the displaced fluid that rotates the shaft connected to flywheel by 360°, and A_p is the piston area [8].

S2 Main-Chain Wave Speed & Dimensionless Frequency

Considering the one dimensional mono-atomic chain depicted in Fig. 2(a) of the main text, we start with the equations of motion

$$M\ddot{u}_n^M + K(u_n^M - u_{n-1}^M) + K(u_n^M - u_{n+1}^M) = 0 \tag{S1}$$

Here, M is mass on the main chain; K is stiffness on the main chain; and u_n^M is displacement of the n^{th} cell on main chain.

According to the Bloch theorem [5],

$$u_n^M = U^M e^{i(qna+\omega t)} \tag{S2}$$

where U^M is the wave amplitude. Here q, a, ω and t denote the (angular) wave number, lattice constant, (angular) frequency and time, respectively.
From Eqns. (S1) and (S2), we arrive at the classical mono-atomic chain dispersion relation:

$$\omega = 2\sqrt{\frac{K}{M}}\left|\sin(\frac{qa}{2})\right| \tag{S3}$$

Taking the positive-q branch, we can obtain the main-chain wave speed at the long wavelength limit as c = phase velocity $(q \to 0)$ = group velocity $(q \to 0)$.

$$\text{Phase velocity} : v_p(q \to 0) = \lim_{q\to 0}\frac{\omega}{q} = a\sqrt{\frac{K}{M}}\lim_{\frac{qa}{2}\to 0}\frac{\sin(\frac{qa}{2})}{\frac{qa}{2}} \tag{S4}$$

$$\text{Group velocity} : v_g(q \to 0) = \lim_{q\to 0}\frac{d\omega}{dq} = a\sqrt{\frac{K}{M}}\lim_{\frac{qa}{2}\to 0}\cos(\frac{qa}{2}) \tag{S5}$$

Since $\lim_{x\to 0}\frac{\sin x}{x} = 1$ and $\cos(0) = 1$, we arrive at:

$$c = v_p(q \to 0) = v_g(q \to 0) = a\sqrt{\frac{K}{M}} \tag{S6}$$

At the long-wavelength dispersionless limit of $\lambda \gg a$, we also know $c = \omega\lambda/2\pi$. Hence, we arrive at the dimensionless frequency as:

$$f = \frac{\omega a}{2\pi c} = \frac{\omega}{2\pi\sqrt{K/M}} = \frac{a}{\lambda} \tag{S7}$$

S3 Metamaterials with Embedded Inerters

Considering the one dimensional chain depicted in Fig. 2(b) of the main text, we start with the equations of motion

$$M\ddot{u}_n^M + K(u_n^M - u_{n+1}^M) + K(u_n^M - u_{n-1}^M) + b(\ddot{u}_n^M - \ddot{u}_{n-1}^b) + k_b(u_n^M - u_n^b) = 0 \tag{S8}$$

$$k_b(u_n^b - u_n^M) + b(\ddot{u}_n^b - \ddot{u}_{n+1}^M) = 0 \tag{S9}$$

Here, b is inertance; K and k_b are stiffness on the main chain and on the branch chain, respectively; and u_n^M and u_n^b represent displacements of mass M of the n^{th} cell and the degree of freedom on the branch chain connected to the n^{th} cell, respectively.

According to the Bloch theorem [5],

$$u_n^M = U^M e^{i(nqa+\omega t)} \tag{S10}$$

$$u_n^b = U^b e^{i(nqa+\omega t)} \tag{S11}$$

where U^M and U^b are amplitudes of the harmonic waves [15] u_n^M and u_n^b, respectively; q, a, ω and t are wave number, lattice constant, angular frequency and time, respectively.

Substituting Eqns. (S10) and (S11) into Eqns. (S8) and (S9), we get

$$-\omega^2 \begin{bmatrix} M+b & -be^{-iqa} \\ -be^{iqa} & b \end{bmatrix} + \begin{bmatrix} 2K - K(e^{iqa} + e^{-iqa}) + k_b & -k_b \\ -k_b & k_b \end{bmatrix} = \begin{bmatrix} 0 \\ 0 \end{bmatrix} \tag{S12}$$

Fig. S2 shows the dispersion relation can be obtained solving eigenvalue problem using the Eqn. (S12) and when solved analytically can result in dispersion equation for angular frequency which can be used to find the expression for the edges of the band gap [1].

S3.1 Lower Edge of Band Gap

Based on the results plotted in Fig. 2(c) of the main text, we can find the lower edge of the band gap at $q = \pi$, where Eqn. (S12) becomes:

$$-\omega^2 \begin{bmatrix} M+b & b \\ b & b \end{bmatrix} + \begin{bmatrix} 4K + k_b & -k_b \\ -k_b & k_b \end{bmatrix} = \begin{bmatrix} 0 \\ 0 \end{bmatrix} \tag{S13}$$

Taking the smaller eigen-frequency, we arrive at the lower edge frequency ω_{L}:

$$\omega_{\mathrm{L}} = \sqrt{\frac{(4k_bb + k_bM + 4Kb) - \sqrt{(4k_bb + k_bM + 4Kb)^2 - 4(Mb)(4Kk_b)}}{2Mb}} \tag{S14}$$

Eqn. (S14) can be normalized by $2\pi\sqrt{K/M}$:

$$f_{\mathrm{L}} = \frac{1}{2\pi}\sqrt{\frac{(4k_bb + k_bM + 4Kb) - \sqrt{(4k_bb + k_bM + 4Kb)^2 - 4(Mb)(4Kk_b)}}{2Kb}} \tag{S15}$$

Taking stiffness ratio: $\kappa_b = k_b/K$ and inertance: $\mu_b = b/M$, we get:

$$\begin{aligned} f_{\mathrm{L}} &= \frac{1}{2\pi}\sqrt{\chi_b - \sqrt{\chi_b^2 - 4\frac{\kappa_b}{\mu_b}}}, \\ &\text{where,} \\ \chi_b &= 2\kappa_b + \frac{\kappa_b}{2\mu_b} + 2. \end{aligned} \tag{S16}$$

S3.2 Upper Edge of Band Gap

Similarly, we can find the upper edge of the band gap at $q = 0$, where Eqn. (S12) becomes:

$$-\omega^2 \begin{bmatrix} M+b & -b \\ -b & b \end{bmatrix} + \begin{bmatrix} k_b & -k_b \\ -k_b & k_b \end{bmatrix} = 0 \tag{S17}$$

Taking the larger eigen-frequency, we arrive at the upper edge frequency ω_{U}:

$$\omega_{\mathrm{U}} = \sqrt{\frac{k_b}{b}} \tag{S18}$$

Eqn. (S18) can be normalized by $2\pi\sqrt{K/M}$:

$$f_{\mathrm{U}} = \frac{1}{2\pi}\sqrt{\frac{Mk_b}{Kb}} \tag{S19}$$

Taking $\kappa_b = k_b/K$ and $\mu_b = b/M$, we get:

$$f_{\mathrm{U}} = \frac{1}{2\pi}\sqrt{\frac{\kappa_b}{\mu_b}} \tag{S20}$$

S3.3 Convergence Limit for $\mu_b \gg \kappa_b$

Fig. 2(f) of the main text shows that, as inertance becomes large, the size of band gap asymptotically reaches a plateau. For $\mu_b \gg \kappa_b$, Eqns. (S20) and (S16) becomes:

$$f_{\mathrm{U}} = \frac{\sqrt{\zeta}}{2\pi}, \tag{S21}$$

where $\zeta = \kappa_b/\mu_b$.

$$\omega_{\mathrm{L}}^2 = \left(2\pi f_{\mathrm{L}}\right)^2 = \chi_b'' - \sqrt{\chi_b''^{\,2} - 4\zeta} = \chi_b''\left(1 - \sqrt{1-\zeta'}\right) \tag{S22}$$

where $\chi_b'' = 2\kappa_b + 2$, $\zeta = \kappa_b/\mu_b$ and $\zeta' = 4\zeta/\chi_b''^{\,2}$.

The Taylor series expansion of $\sqrt{1-x}$ is:

$$\sqrt{1-x} = \sum_{n=0}^{\infty} x^n (-1)^n \binom{\frac{1}{2}}{n} = 1 - \frac{x}{2} - \frac{x^2}{8} - \frac{x^3}{16} \ldots \tag{S23}$$

The first two terms of the Taylor series from Eqn. (S23) are significant. Hence, from Eqns. (S22) and (S23) we arrive at:

$$\omega_{\mathrm{L}}^2 = \left(2\pi f_{\mathrm{L}}\right)^2 \to \chi_b''\left(1 - \left(1 - \frac{\zeta'}{2}\right)\right) = \chi_b''\frac{\zeta'}{2} = \frac{2\zeta}{\chi_b''} \tag{S24}$$

$$f_{\mathrm{L}} \to \frac{1}{2\pi}\sqrt{\frac{2\zeta}{\chi_b''}} = \frac{1}{2\pi}\sqrt{\frac{\kappa_b}{\mu_b(\kappa_b+1)}} \tag{S25}$$

For $\kappa_b = 1$, the relative size of band gap converges to:

$$\Delta f = \frac{f_{\mathrm{U}} - f_{\mathrm{L}}}{f_{\mathrm{L}}} \to \frac{\sqrt{\zeta} - \sqrt{2\zeta/\chi_b''}}{\sqrt{2\zeta/\chi_b''}} = \sqrt{\kappa_b + 1} - 1 = 41.4\% \tag{S26}$$

S3.4 Additional convergence Limit for $\kappa_b \gg 1$

Fig. 2(g) of the main text shows that, as stiffness ratio becomes large, the lower edge of the band gap shifts to higher frequency and then converges to a finite limit. For $\kappa_b \gg 1$, Eqn. (S16) becomes:

$$\begin{aligned}
&\left(2\pi f_{\mathrm{L}}\right)^2 = \chi_b' - \sqrt{{\chi_b'}^2 - \Upsilon} = \chi_b'\left(1 - \sqrt{1 - \Upsilon'}\right) \\
&\text{where,} \\
&\chi_b' = 2\kappa_b \\
&\Upsilon = 4\kappa_b/\mu_b \\
&\Upsilon' = \Upsilon/{\chi_b'}^2 = (\kappa_b\,\mu_b)^{-1}
\end{aligned} \tag{S27}$$

The first two terms of the Taylor series from Eqn. (S23) are significant. Hence, from Eqns. (S27) and (S23) we arrive at:

$$\left(2\pi f_{\mathrm{L}}\right)^2 \to \chi_b'\left(1 - \left(1 - \frac{\Upsilon'}{2}\right)\right) = \chi_b'\frac{\Upsilon'}{2} = \frac{1}{\mu_b} \tag{S28}$$

For $\mu_b = 10^6$, the lower edge of the band gap converges to:

$$f_{\mathrm{L}} \to \frac{1}{2\pi}\sqrt{\frac{1}{\mu_b}} = 1.59 \times 10^{-4} \tag{S29}$$

From Eqns. (S20) and (S29) the relative gap size converges to:

$$\Delta f = \frac{f_{\mathrm{U}} - f_{\mathrm{L}}}{f_{\mathrm{L}}} \to \frac{\sqrt{\kappa_b/\mu_b} - \sqrt{1/\mu_b}}{\sqrt{1/\mu_b}} = \sqrt{\kappa_b} - 1 \to \sqrt{\kappa_b} \tag{S30}$$

S3.5 Eigenvector Formulation

Components of eigenvector U^M and U^b can be defined using Eqn.(S12):

$$\begin{bmatrix} -\omega^2(M+b) + 2K - K(e^{iqa} + e^{-iqa}) + k_b & \omega^2 b e^{-iqa} - k_b \\ \omega^2 b e^{iqa} - k_b & -\omega^2 b + k_b \end{bmatrix} \begin{Bmatrix} U^M \\ U^b \end{Bmatrix} = \begin{bmatrix} 0 \\ 0 \end{bmatrix} \tag{S31}$$

S3.6 Modal Displacement Ratio at Lower Gap Edge

Solving Eqn.(S31) for eigenvector,

$$U^b = \frac{-\omega^2(M+b) + 2K - K(e^{iqa} + e^{-iqa}) + k_b}{-\omega^2 b e^{-iqa} + k_b} U^M \tag{S32}$$

From Eqns.(S14) and (S32), modal displacement ratio at the lower edge of the band gap, i.e., $q = \pi$,

$$\begin{aligned} &\frac{U^b}{U^M} = \frac{-\omega_{\mathrm{L}}^2(M+b) + 4K + k_b}{\omega_{\mathrm{L}}^2 b + k_b} \\ &\text{where,} \\ &\omega_{\mathrm{L}}^2 = \chi_b - \sqrt{\chi_b^2 - \frac{4Kk_b}{Mb}} \\ &\chi_b = \frac{2k_b}{M} + \frac{k_b}{2b} + \frac{2K}{M} \end{aligned} \tag{S33}$$

Eqn. (S33) is the expression for modal displacement ratio at the lower edge frequency of the band gap.

S3.7 Modal Displacement Ratio at Upper Gap Edge

Solving Eqn.(S31) for eigenvector,

$$U^b = \frac{-\omega^2 b e^{iqa} + k_b}{-\omega^2 b + k_b} U^M \tag{S34}$$

From Eqns.(S18) and (S34), modal displacement ratio at the upper edge of the band gap, i.e., $q = 0$,

$$\frac{U^b}{U^M} = 1 \tag{S35}$$

Eqn. (S35) is the expression for modal displacement ratio at the upper edge frequency of the band gap.

S3.8 Continuum Model

A continuum mechanics-based model on the basis of the discrete lattice model can be obtained by replacing discrete parts with their equivalent continuum counterparts [4].

The approximations of the discrete elements in Eqns. (S8) and (S9) are:

$$\begin{aligned}
u_n^M &= u^M(x) \\
u_{n+1}^M &= u^M(x+a) = u^M(x) + \frac{a}{1!}\frac{\partial u^M}{\partial x} + \frac{a^2}{2!}\frac{\partial^2 u^M}{\partial x^2} + \dots \\
u_{n-1}^M &= u^M(x-a) = u^M(x) - \frac{a}{1!}\frac{\partial u^M}{\partial x} + \frac{a^2}{2!}\frac{\partial^2 u^M}{\partial x^2} + \dots \\
u_n^b &= u^b(x) \\
u_{n+1}^b &= u^b(x+a) = u^b(x) + \frac{a}{1!}\frac{\partial u^b}{\partial x} + \frac{a^2}{2!}\frac{\partial^2 u^b}{\partial x^2} + \dots \\
u_{n-1}^b &= u^b(x-a) = u^b(x) - \frac{a}{1!}\frac{\partial u^b}{\partial x} + \frac{a^2}{2!}\frac{\partial^2 u^b}{\partial x^2} + \dots
\end{aligned} \tag{S36}$$

From Eqns. (S8), (S9) and (S36), we arrive at:

$$\begin{aligned}
(-\omega^2 M - a^2 q^2 K + k_b)u^M(x) - (\omega^2\left(aq - \frac{a^2q^2}{2}\right)b + k_b)u^b(x) = 0 \\
(\omega^2\left(1 + aq + \frac{a^2q^2}{2}\right)b - k_b)u^M(x) - (\omega^2 b - k_b)u^b(x) = 0
\end{aligned} \tag{S37}$$

Dispersion relation for continuum model is obtained solving Eqn. (S37):

$$\omega = \sqrt{\frac{2(Mk_b - Kba^2q^2 - k_bba^2q^2) \pm 2\sqrt{\begin{array}{l}M^2k_b^2 + 2(K-k_b)bk_ba^2q^2 \\ \quad + (K+k_b)^2b^2a^4q^4 - Kk_ba^6q^6\end{array}}}{4Mb - a^4q^4}} \tag{S38}$$

Normalizing Eqn.(S38) by $2\pi\sqrt{K/M}$,

$$f = \frac{1}{2\pi}\sqrt{\frac{M}{K}}\sqrt{\frac{2(Mk_b - Kba^2q^2 - k_bba^2q^2) \pm 2\sqrt{\begin{array}{l}M^2k_b^2 + 2(K-k_b)bk_ba^2q^2 \\ \quad + (K+k_b)^2b^2a^4q^4 - Kk_ba^6q^6\end{array}}}{4Mb - a^4q^4}} \tag{S39}$$

Continuum model, obtained using Eqn. (S38), is in close agreement with the discrete model, obtained solving the eigenvalue problem for Eqn. (S12) (shown in Fig. S2) for the bandgap region. Higher-order continuum model can lead to better agreement between the two models for complete dispersion curve.

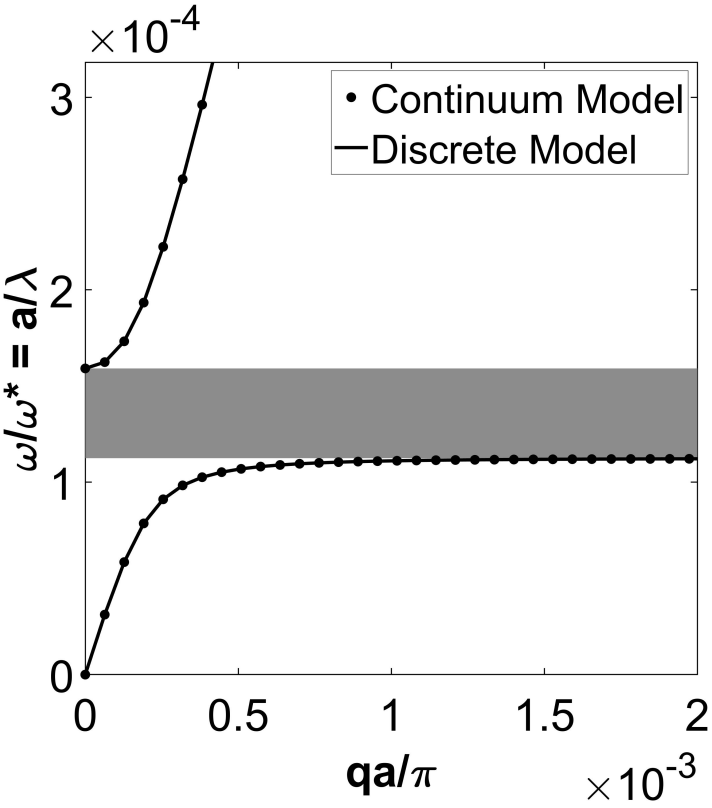

Figure S2: Comparison between two-order continuum model and discrete model.

S4 Metamaterials with Inerter-Mass-Resonators

Considering the one dimensional chain depicted in Fig. 4(a) of the main text, we start with the equations of motion

$$M\ddot{u}_n^M + K(u_n^M - u_{n+1}^M) + K(u_n^M - u_{n-1}^M) + k_f(u_n^M - u_n^m) + k_b(u_n^M - u_n^b) = 0 \tag{S40}$$

$$m\ddot{u}_n^m + k_f(u_n^m - u_n^M) + b(\ddot{u}_n^m - \ddot{u}_{n+1}^b) = 0 \tag{S41}$$

$$k_b(u_n^b - u_n^M) + b(\ddot{u}_n^b - \ddot{u}_{n+1}^m) = 0 \tag{S42}$$

Here, b is inertance; K is stiffness on the main chain and k_f and k_b are stiffness on the branch chain; and u_n^M and u_n^m represent displacements of main chain mass, M, and resonator chain mass, m of the n^{th} cell and u_n^b is the degree of freedom on the branch chain connected to the n^{th} cell.

According to the Bloch theorem [5],

$$u_n^M = U^M e^{i(nqa+\omega t)} \tag{S43}$$

$$u_n^m = U^m e^{i(nqa+\omega t)} \tag{S44}$$

$$u_n^b = U^b e^{i(nqa+\omega t)} \tag{S45}$$

where U^M, U^m and U^b are amplitudes of the harmonic waves [15] u_n^M, u_n^m and u_n^b, respectively; q, a, ω and t are wave number, lattice constant, angular frequency and time, respectively.

Substituting Eqns. (S43), (S44) and (S45) into Eqns. (S40), (S41) and (S42), we get

$$-\omega^2 \begin{bmatrix} M & 0 & 0 \\ 0 & m+b & -b \\ 0 & -b & b \end{bmatrix} + \begin{bmatrix} 2K - K(e^{iqa} + e^{-iqa}) + k_f + k_b & -k_f & -k_b \\ -k_f & k_f & 0 \\ -k_b & 0 & k_b \end{bmatrix} = \begin{bmatrix} 0 \\ 0 \\ 0 \end{bmatrix} \tag{S46}$$

Fig. S3 shows the dispersion relation can be obtained solving eigenvalue problem using the Eqn. (S46) and when solved analytically can result in dispersion equation for angular frequency which can be used to find the expression for the edges of the band gap [1]. As Eqn. (S46) suggests there are three degrees of freedom, so there will be three frequency bands which produces two band gaps, one in higher frequency regime and one in low frequency regime. The rest of the study for this section focuses on the lower band gap.

S4.1 Lower Edge of Band Gap

Based on the results plotted in Fig. S3, we can find the lower edge of the band gap at $q = \pi/a$, where Eqn. (S46) becomes:

$$-\omega^2 \begin{bmatrix} M & 0 & 0 \\ 0 & m+b & -b \\ 0 & -b & b \end{bmatrix} + \begin{bmatrix} 4K + k_f + k_b & -k_f & -k_b \\ -k_f & k_f & 0 \\ -k_b & 0 & k_b \end{bmatrix} = \begin{bmatrix} 0 \\ 0 \\ 0 \end{bmatrix} \tag{S47}$$

The cubic polynomial in Eqn. S48 can be solved analytically and the smallest eigen-frequency can be used to arrive at the lower gap edge frequency ω_{L}:

$$A\lambda^3 + B\lambda^2 + C\lambda + D = 0 \tag{S48}$$

where,

$$\begin{aligned} A &= -Mmb \\ B &= k_f Mb + k_b M(m+b) + bm(k_f + k_b) + 4Kbm \\ C &= k_f k_b (M+m) - 4K(k_f b + k_b m + k_b b) \\ D &= 4Kk_f k_b \\ \lambda &= \omega^2 \\ \omega_{\mathrm{L}} &= \sqrt{\lambda_{\min}} \end{aligned} \tag{S49}$$

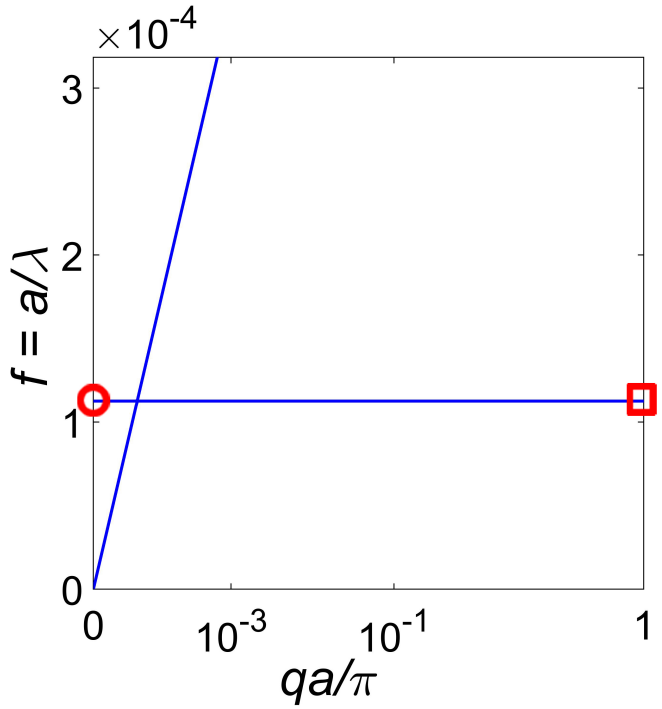

Figure S3: (a) Dispersion curve for material with inerter-mass-resonator shows no band gap for $m/M = 1$, $b/m_b = b/M = 10^6$ and $k_b/K = k_f/K = 1$. Here, the frequency is normalized with respect to $2\pi c/a = 2\pi\sqrt{K/M}$, so that $f = a/\lambda$. The red square shows the frequency at the lower edge of the band gap. The red circle shows the frequency of the upper edge of the band gap. λ: wavelength, a: unit cell length, K: spring stiffness on main chain, M: mass on main chain, k_f and k_b: spring stiffness on resonator chain.

S4.2 Upper Edge of Band Gap

Similarly, we can find the upper edge of the band gap at $q = 0$, where Eqn. (S46) becomes:

$$-\omega^2 \begin{bmatrix} M & 0 & 0 \\ 0 & m+b & -b \\ 0 & -b & b \end{bmatrix} + \begin{bmatrix} k_f + k_b & -k_f & -k_b \\ -k_f & k_f & 0 \\ -k_b & 0 & k_b \end{bmatrix} = \begin{bmatrix} 0 \\ 0 \\ 0 \end{bmatrix} \tag{S50}$$

Taking the second eigen-frequency (the first one is zero), we arrive at the upper gap edge frequency ω_{U}:

$$\omega_{\mathrm{U}} = \sqrt{\frac{-\begin{pmatrix} k_f Mb + k_b M(m+b) \\ + bm(k_f + k_b) \end{pmatrix} + \sqrt{\begin{matrix} (k_f Mb + k_b M(m+b) + bm(k_f + k_b))^2 \\ + 4(Mmb)k_f k_b (M+m) \end{matrix}}}{-2Mmb}} \tag{S51}$$

Eqn. (S51) can be normalized by $2\pi\sqrt{K/M}$:

$$f_{\mathrm{U}} = \frac{1}{2\pi}\sqrt{\frac{-\begin{pmatrix} k_f Mb \\ + k_b M(m+b) \\ + bm(k_f + k_b) \end{pmatrix} + \sqrt{\begin{matrix} (k_f Mb + k_b M(m+b) + bm(k_f + k_b))^2 \\ + 4(Mmb)k_f k_b (M+m) \end{matrix}}}{-2Kmb}} \tag{S52}$$

Taking $\kappa_f = k_f/K$, $\kappa_b = k_b/K$, $\mu_b = b/M$ and $\mu_m = m/M$, we get:

$$\begin{aligned} f_{\mathrm{U}} &= \frac{1}{2\pi}\sqrt{\chi_f - \sqrt{\chi_f^2 - \frac{\kappa_f \kappa_b}{\mu_b}\left(\frac{1}{\mu_m} + 1\right)}}, \\ &\text{where} \\ \chi_f &= \frac{\kappa_f}{2}\left(\frac{1}{\mu_m} + 1\right) + \frac{\kappa_b}{2}\left(\frac{1}{\mu_b} + \frac{1}{\mu_m} + 1\right). \end{aligned} \tag{S53}$$

S4.3 Convergence Limit for $b \gg M, m, K, k_f, k_b$

Fig. S4 shows that, as inertance becomes large, the size of the band gap asymptotically approaches zero. Here, we consider the limit of large inertance $b \gg M, m, K, k_f, k_b$, and low frequency $\omega_{\mathrm{L}} \ll 1$, i.e. $\lambda \ll 1$, Eqn. (S49) becomes:

$$\begin{aligned} A &= -Mmb \\ B &= (k_f + k_b)(M+m)b + 4Kmb \\ C &= -4K(k_f + k_b)b \end{aligned} \tag{S54}$$

Eqn. (S48) becomes:

$$\begin{aligned} &-4K(k_f + k_b)b\lambda + 4Kk_f k_b = 0 \\ &\sqrt{\lambda} = \omega_{\mathrm{L}} = \sqrt{\frac{k_f k_b}{(k_f + k_b)b}} \end{aligned} \tag{S55}$$

For $\mu_b \gg \mu_m$, $\mu_b \gg \kappa_b$ and $\mu_b \gg \kappa_f$ we have

$$\begin{aligned}&\left(2\pi f_{\mathrm{U}}\right)^2 = \chi_f' - \sqrt{{\chi_f'}^2 - 2\zeta} = \chi_f'\left(1 - \sqrt{1-\zeta'}\right).\\ &\text{where}\\ &\chi_f' = \kappa_f + \kappa_b,\\ &\zeta = \kappa_f\kappa_b/\mu_b,\\ &\zeta' = 2\zeta/{\chi_f'}^2.\end{aligned} \tag{S56}$$

We also have

$$\begin{aligned}&\omega_{\mathrm{L}} = \frac{\omega^*}{2\pi}\sqrt{\frac{\zeta}{\chi_f'}},\\ &\text{where}\\ &\chi_f' = \kappa_f + \kappa_b,\\ &\zeta = \kappa_f\kappa_b/\mu_b,\\ &\zeta' = 2\zeta/{\chi_f'}^2.\end{aligned} \tag{S57}$$

The first two terms of the Taylor series from Eqn. (S23) are significant. Hence, from Eqns. (S56) and (S23) we arrive at:

$$\left(2\pi f_{\mathrm{U}}\right)^2 = \chi_f'\left(1 - \left(1 - \frac{\zeta'}{2}\right)\right) = \chi_f'\frac{\zeta'}{2} = \frac{\zeta}{\chi_f'} \tag{S58}$$

$$\omega_{\mathrm{U}} = \frac{\omega^*}{2\pi}\sqrt{\frac{\zeta}{\chi_f'}} \tag{S59}$$

Eqns. (S57) and (S59) can be used to find the convergence of the band gap size:

$$\Delta f = \frac{f_{\mathrm{U}} - f_{\mathrm{L}}}{f_{\mathrm{L}}} = \frac{\sqrt{\zeta/\chi_f'} - \sqrt{\zeta/\chi_f'}}{\sqrt{\zeta/\chi_f'}} = 0\% \tag{S60}$$

S4.4 Possibility of Ultra-low Frequency Band Gap

As shown by the limit analysis above, having a large inertance will unavoidably close the band gap in this case. This fact is further corroborated by the numerical results shown in Fig. S4(b). Consequently, we conclude that metamaterials with inerter-mass-resonators cannot achieve band gap at ultra-low frequency.

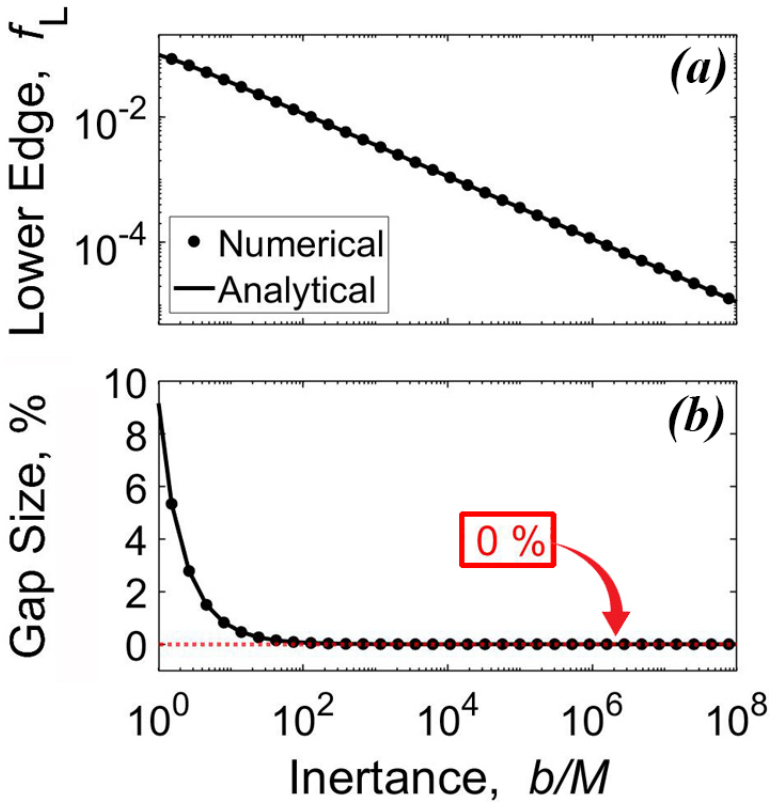

Figure S4: (a) and (b) show lower edge and relative size for $k_f/K = 1$, $m/M = 1$ and $k_m/K = 1$.

S5 Metamaterials with Mass-Resonators

Considering the one dimensional chain depicted in Fig. 4(b) of the main text, we start with the equations of motion

$$M\ddot{u}_n^M + K(u_n^M - u_{n+1}^M) + K(u_n^M - u_{n-1}^M) + k_m(u_n^M - u_n^m) = 0 \tag{S61}$$

$$m\ddot{u}_n^m + k_m(u_n^m - u_n^M) = 0 \tag{S62}$$

Here, M and m are masses on the main chain and branch chain, respectively; K and k_m are stiffness on the main chain and branch chain, respectively; and u_n^M and u_n^m are displacements of the n^{th} cell on main chain and branch chain, respectively.

According to the Bloch theorem [5, 15],

$$u_n^M = U^M e^{i(nqa+\omega t)} \tag{S63}$$

$$u_n^m = U^m e^{i(nqa+\omega t)} \tag{S64}$$

where U^M and U^m are vibration amplitudes of M and m, respectively; q, a, ω and t are (angular) wave number, lattice constant, (angular) frequency and time, respectively.

Substituting Eqns. S63 and S64 into Eqns. S61 and S62, we get

$$-\omega^2 \begin{bmatrix} M & 0 \\ 0 & m \end{bmatrix} + \begin{bmatrix} 2K - K(e^{iqa} + e^{-iqa}) + k_m & -k_m \\ -k_m & k_m \end{bmatrix} = \begin{bmatrix} 0 \\ 0 \end{bmatrix} \tag{S65}$$

Dispersion relation can be obtained analytically solving the Eqn. (S65) which can be used to find the expression for the edges of the band gap [1].

S5.1 Lower Edge of Band Gap

We can find the lower edge of the band gap at $q = \pi/a$, where Eqn. (S65) becomes:

$$-\omega^2 \begin{bmatrix} M & 0 \\ 0 & m \end{bmatrix} + \begin{bmatrix} 4K + k_m & -k_m \\ -k_m & k_m \end{bmatrix} = \begin{bmatrix} 0 \\ 0 \end{bmatrix} \tag{S66}$$

Taking the smaller eigen-frequency, we arrive at the lower edge frequency ω_{L}:

$$\omega_{\mathrm{L}} = \sqrt{\frac{(4Km + k_m m + k_m M) - \sqrt{(4Km + k_m m + k_m M)^2 - 4(Mm)(4Kk_m)}}{2Mm}} \tag{S67}$$

Eqn. (S67) can be normalized by $2\pi\sqrt{K/M}$:

$$f_{\mathrm{L}} = \frac{1}{2\pi}\sqrt{\frac{(4Km + k_m m + k_m M) - \sqrt{(4Km + k_m m + k_m M)^2 - 4(Mm)(4Kk_m)}}{2Km}} \tag{S68}$$

Taking $\kappa_m = k_m/K$ and $\mu_m = m/M$, we get:

$$f_{\mathrm{L}} = \frac{1}{2\pi}\sqrt{\chi_m - \sqrt{\chi_m^2 - 4\frac{\kappa_m}{\mu_m}}}$$
$$\text{where,} \tag{S69}$$
$$\chi_m = 2 + \frac{\kappa_m}{2} + \frac{\kappa_m}{2\mu_m}$$

S5.2 Upper Edge of Band Gap

Similarly, we can find the upper edge of the band gap at q=0, where Eqn. (S65) becomes:

$$-\omega^2 \begin{bmatrix} M & 0 \\ 0 & m \end{bmatrix} + \begin{bmatrix} k_m & -k_m \\ -k_m & k_m \end{bmatrix} = 0 \tag{S70}$$

Taking the larger eigen-frequency, we arrive at the upper edge frequency ω_{U}:

$$\omega_{\mathrm{U}} = \sqrt{\frac{k_m(M+m)}{Mm}} \tag{S71}$$

Eqn. (S71) can be normalized by $2\pi\sqrt{K/M}$:

$$f_{\mathrm{U}} = \frac{1}{2\pi}\sqrt{\frac{k_m(M+m)}{Km}} \tag{S72}$$

Taking $\kappa_m = k_m/K$ and $\mu_m = m/M$, we get:

$$f_{\mathrm{U}} = \frac{1}{2\pi}\sqrt{\frac{\kappa_m}{\mu_m} + \kappa_m} \tag{S73}$$

S5.3 Convergence Limit for $\mu_m \gg \kappa_m$

As resonator mass becomes large, the size of band gap goes to infinity. For $\mu_m \gg \kappa_m$, Eqns. (S69) and (S73) becomes:

$$f_{\mathrm{U}} = \frac{1}{2\pi}\sqrt{\zeta + \kappa_m} \quad \text{where} \quad \zeta = \kappa_m/\mu_m, \tag{S74}$$

$$\omega_{\mathrm{L}}^2 = \left(2\pi f_{\mathrm{L}}\right)^2 = \chi'_m - \sqrt{(\chi'_m)^2 - 4\zeta} = \chi'_m\left(1 - \sqrt{1-\zeta'}\right), \tag{S75}$$

where $\chi'_m = 2 + \kappa_m/2$, $\zeta = \kappa_m/\mu_m$, and $\zeta' = 4\zeta/(\chi'_m)^2$.
The first two terms of Taylor series from Eqn. (S23) are significant. Hence, from Eqns.(S75) and (S23) we arrive at:

$$\omega_{\mathrm{L}}^2 = \left(2\pi f_{\mathrm{L}}\right)^2 \to \chi'_m\left(1 - \left(1 - \frac{\zeta'}{2}\right)\right) = \chi'_m\frac{\zeta'}{2} = \frac{2\zeta}{\chi'_m} \tag{S76}$$

$$f_{\mathrm{L}} \to \frac{1}{2\pi}\sqrt{\frac{2\zeta}{\chi'_m}} = \frac{1}{2\pi}\sqrt{\frac{4\kappa_m}{\mu_m(4+\kappa_m)}} \tag{S77}$$

The relative band gap size converges to:

$$\Delta f = \frac{f_{\mathrm{U}} - f_{\mathrm{L}}}{f_{\mathrm{L}}} \to \frac{\sqrt{\zeta+\kappa_m} - \sqrt{2\zeta/\chi'_m}}{\sqrt{2\zeta/\chi'_m}} = \sqrt{\frac{\chi'_m}{2}(\mu_m+1)} - 1 \to \sqrt{\mu_m + \frac{\kappa_m\mu_m}{4} + 1} - 1 \tag{S78}$$

S5.4 Eigenvector Formulation

Components of eigenvector U^M and U^m can be defined using Eqn. (S70):

$$\begin{bmatrix} -\omega^2 M + 2K - K(e^{iqa} + e^{-iqa}) + k_m & -k_m \\ -k_m & -\omega^2 m + k_m \end{bmatrix} \begin{Bmatrix} U^M \\ U^m \end{Bmatrix} = \begin{bmatrix} 0 \\ 0 \end{bmatrix} \tag{S79}$$

S5.5 Modal Displacement Ratio at Lower Gap Edge

Solving Eqn. (S79) for $\omega = \omega_{\mathrm{L}}$, we get:

$$U^m = \frac{-\omega^2 M + 4K + k_m}{k_m} U^M \tag{S80}$$

From Eqns. (S67) and (S80),

$$\frac{U^m}{U^M} = -\frac{(4Km + k_m m + k_m M) - \sqrt{\begin{matrix}(4Km + k_m m + k_m M)^2 \\ -\,4(Mm)(4Kk_m)\end{matrix}}}{2mk_m} + \frac{4K}{k_m} + 1 \tag{S81}$$

Taking $\kappa_m = k_m/K$ and $\mu_m = m/M$, we get

$$\begin{aligned} &\frac{U^m}{U^M} = \chi_m + \sqrt{\chi_m^2 - \frac{4}{\mu_m\kappa_m}}, \\ &\text{where} \\ &\chi_m = \frac{2}{\kappa_m} + \frac{1}{2} - \frac{1}{2\mu_m} \end{aligned} \tag{S82}$$

S5.6 Convergence Limit of Modal Displacement Ratio

For $\kappa_m \ll \mu_m$, Eqn. (S82) becomes:

$$\begin{aligned} &\frac{U^m}{U^M} = \chi'_m + \sqrt{{\chi'_m}^2 - 4\Upsilon} = \chi'_m\left(1 + \sqrt{1-\Upsilon'}\right), \\ &\text{where} \\ &\chi'_m = 2/\kappa_m \\ &\Upsilon = (\mu_m\,\kappa_m)^{-1} \\ &\Upsilon' = 4\Upsilon/{\chi'_m}^2 \end{aligned} \tag{S83}$$

The first two terms of the Taylor series from Eqn. (S23) are significant. Hence, from Eqns.(S83) and (S23) we arrive at:

$$\frac{U^m}{U^M} = \chi'_m\left(1 + \left(1 - \frac{\Upsilon'}{2}\right)\right) = 2\chi'_m + \frac{2\Upsilon}{\chi'_m} = \frac{4}{\kappa_m} - \frac{1}{\mu_m} = 8 \times 10^6 \tag{S84}$$

S5.7 Modal Displacement Ratio at Upper Gap Edge

Solving Eqn. (S79) for $\omega = \omega_{\mathrm{U}}$, we get:

$$U^m = \frac{k_m}{-\omega^2 m + k_m} U^M \tag{S85}$$

From Eqns. (S71) and (S85),

$$\frac{U^m}{U^M} = -\frac{M}{m} \tag{S86}$$

Taking $\mu_m = m/M$, we get:

$$\frac{U^m}{U^M} = -\frac{1}{\mu_m} \tag{S87}$$

Eqn. S87 is the expression for modal displacement ratio on the upper edge of the band gap

S6 Steady-State Frequency-Domain Formulation For Finite-Size One-Dimensional Metamaterials with Embedded Inerters

Here, we consider a finite chain of N unit cells (Fig. S5), and only the first mass at u_1^M is being harmonically excited. The equations of motion are:

$$\begin{aligned}
&M\ddot{u}_1^M + K(u_1^M - u_2^M) + k_b(u_1^M - u_1^b) = F_0 e^{i\omega t} \\
&M\ddot{u}_2^M + K(u_2^M - u_1^M) + K(u_2^M - u_3^M) \\
&\qquad\qquad +k_b(u_2^M - u_2^b) + b(\ddot{u}_2^M - \ddot{u}_1^b) = 0 \\
&\vdots \\
&\vdots \\
&M\ddot{u}_{N-1}^M + K(u_{N-1}^M - u_{N-2}^M) + K(u_{N-1}^M - u_N^M) \\
&\qquad\qquad +k_b(u_{N-1}^M - u_{N-1}^b) + b(\ddot{u}_{N-1}^M - \ddot{u}_{N-2}^b) = 0 \\
&M\ddot{u}_N^M + K(u_N^M - u_{N-1}^M) + b(\ddot{u}_N^M - \ddot{u}_{N-1}^b) = 0
\end{aligned} \tag{S88}$$

$$\begin{aligned}
&k_b(u_1^b - u_1^M) + b(\ddot{u}_1^b - \ddot{u}_2^M) = 0 \\
&k_b(u_2^b - u_2^M) + b(\ddot{u}_2^b - \ddot{u}_3^M) = 0 \\
&\vdots \\
&\vdots \\
&k_b(u_{N-2}^b - u_{N-2}^M) + b(\ddot{u}_{N-2}^b - \ddot{u}_{N-3}^M) = 0 \\
&k_b(u_{N-1}^b - u_{N-1}^M) + b(\ddot{u}_{N-1}^b - \ddot{u}_N^M) = 0
\end{aligned} \tag{S89}$$

Taking the solution for Eqns. (S88) and (S89) as:

$$\begin{aligned}
u_N^M &= U_N^M e^{i\omega t} \\
u_N^b &= U_N^b e^{i\omega t}
\end{aligned} \tag{S90}$$

From Eqns. (S88) and (S90) we get,

$$\begin{Bmatrix}
\alpha_1 & \gamma & 0 & \dots & 0 & 0 & \kappa & 0 & \dots & 0 & 0 \\
\gamma & \alpha & \gamma & \dots & 0 & 0 & \delta & \kappa & \dots & 0 & 0 \\
0 & \gamma & \alpha & \dots & 0 & 0 & 0 & \delta & \dots & 0 & 0 \\
\vdots & \vdots & \vdots & \ddots & \vdots & \vdots & \vdots & \vdots & \ddots & \vdots & \vdots \\
0 & 0 & 0 & \dots & \alpha & \gamma & 0 & 0 & \dots & \delta & \kappa \\
0 & 0 & 0 & \dots & \gamma & \alpha_N & 0 & 0 & \dots & 0 & \delta \\
-k_b & \beta_a & 0 & \dots & 0 & 0 & \beta_b & 0 & \dots & 0 & 0 \\
0 & -k_b & \beta_a & \dots & 0 & 0 & 0 & \beta_b & \dots & 0 & 0 \\
\vdots & \vdots & \vdots & \ddots & \vdots & \vdots & \vdots & \vdots & \ddots & \vdots & \vdots \\
0 & 0 & 0 & \dots & \beta_a & 0 & 0 & 0 & \dots & \beta_b & 0 \\
0 & 0 & 0 & \dots & -k_b & \beta_a & 0 & 0 & \dots & 0 & \beta_b
\end{Bmatrix}
\begin{bmatrix}
U_1^M \\ U_2^M \\ U_3^M \\ \vdots \\ U_{N-1}^M \\ U_N^M \\ U_1^b \\ U_2^b \\ \vdots \\ U_{N-2}^b \\ U_{N-1}^b
\end{bmatrix}
=
\begin{bmatrix}
\frac{F_0}{M} \\ 0 \\ 0 \\ \vdots \\ 0 \\ 0 \\ 0 \\ 0 \\ \vdots \\ 0 \\ 0
\end{bmatrix} \tag{S91}$$

where,

$$
\begin{aligned}
\alpha_1 &= -\omega^2 + \frac{K}{M} + \frac{k_b}{M} \\
\alpha &= -\omega^2(1 + \frac{b}{M}) + \frac{2K}{M} + \frac{k_b}{M} \\
\alpha_N &= -\omega^2(1 + \frac{b}{M}) + \frac{K}{M} \\
\gamma &= -\frac{K}{M} \\
\kappa &= -\frac{k_b}{M} \\
\delta &= \omega^2 \frac{b}{M} \\
\beta_a &= \omega^2 b \\
\beta_b &= -\omega^2 b + k_b
\end{aligned}
\tag{S92}
$$

Transmissibility is calculated by:

$$
\text{Transmissibility} = 20\ log\left(\frac{U_N^M}{U_1^M}\right) \tag{S93}
$$

where U_1^M and U_N^M are displacements of mass of the 1^{th} and N^{th} unit cells, respectively. Fig. 1(d) of main text shows frequency domain simulation for inerter-based metamaterial with 10,000 unit cells.

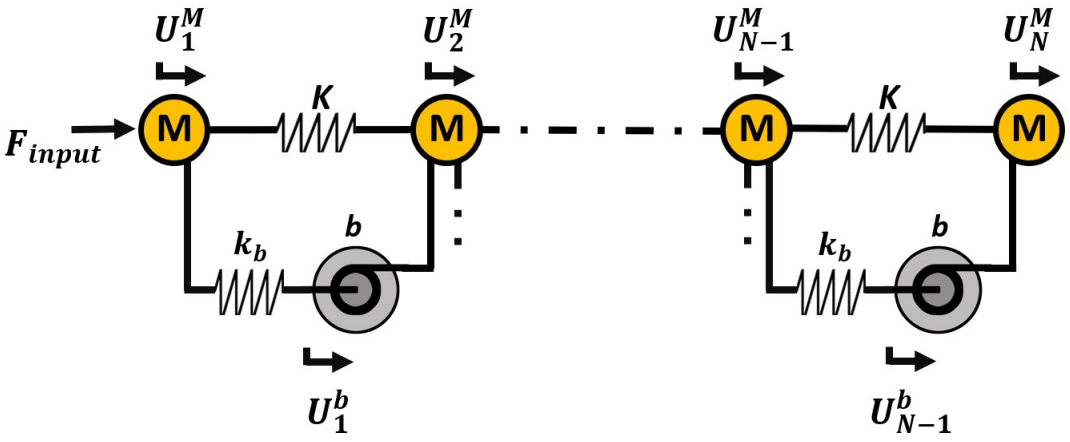

Figure S5: Finite N number of unit cells of inerter-based metamaterial.

Effect of finite number of unit cells has been shown in Fig. S6. As the number of unit cells decreases the drop in transmissibility is less. Fig. S7(a) shows the finite size effect for

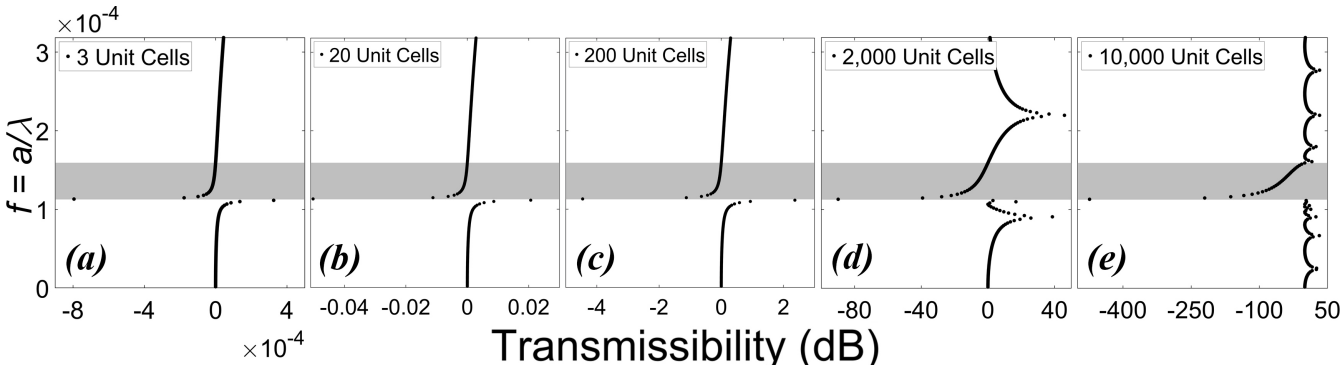

Figure S6: Effect of finite unit cells.

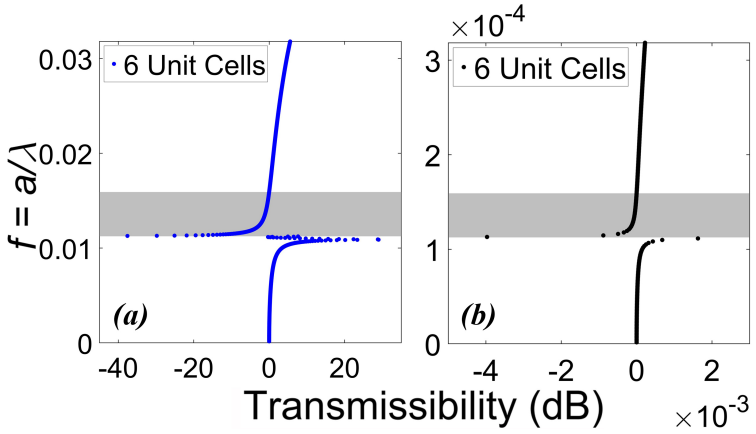

Figure S7: (a) and (b) Effect of finite unit cells in resonator-based and inerter-based metamaterial, respectively.

resonator-based metamaterial for 6 unit cells. Several previous studies [6, 2, 18, 20] show a band gap due to resonator can be realized in practice with despite of the finite size effects. So, for inerter-based metamaterial it is also possible to realize a band gap regardless of the finite size effects (Fig. S7(b)).

S7 Effect of Stiffness k_p Parallel to Inerters in Metamaterials with Embedded Inerters

Considering the one dimensional chain depicted in Fig. S8, we start with the equations of motion

$$M\ddot{u}_n^M + K(u_n^M - u_{n+1}^M) + K(u_n^M - u_{n-1}^M) + k_p(u_n^M - u_{n-1}^b) + b(\ddot{u}_n^M - \ddot{u}_{n-1}^b) + k_b(u_n^M - u_n^b) = 0 \quad \text{(S94)}$$

$$k_b(u_n^b - u_n^M) + k_p(u_n^b - u_{n+1}^M) + b(\ddot{u}_n^b - \ddot{u}_{n+1}^M) = 0 \quad \text{(S95)}$$

Here, b is inertance; K, k_b and k_p are stiffness on the main chain, on the branch chain in series to inerter and on the branch chain in parallel to inerter, respectively; and u_n^M and u_n^b represent displacements of mass M of the n^{th} cell and the degree of freedom on the branch chain connectted to the n^{th} cell, respectively.

Substituting Eqns. (S10) and (S11) into Eqns. (S94) and (S95), we get:

$$-\omega^2 \begin{bmatrix} M+b & -be^{-q} \\ -be^{q} & b \end{bmatrix} + \begin{bmatrix} 2K - K(e^q + e^{-q}) + k_p + k_b & -k_p e^{-q} - k_b \\ -k_b - k_p e^q & k_b + k_p \end{bmatrix} = \begin{bmatrix} 0 \\ 0 \end{bmatrix} \quad \text{(S96)}$$

Dispersion relation can be obtained analytically solving the Eqn. (S96) which can be used to find the expression for the edges of the band gap [1].

S7.1 Lower Edge of the Band Gap

We can find the lower edge of the band gap at $q = \pi$, where Eqn. (S96) becomes:

$$-\omega^2 \begin{bmatrix} M+b & b \\ b & b \end{bmatrix} + \begin{bmatrix} 4K + k_b + k_p & -k_b + k_p \\ -k_b + k_p & k_b + k_p \end{bmatrix} = \begin{bmatrix} 0 \\ 0 \end{bmatrix} \quad \text{(S97)}$$

Taking the smaller eigen-frequency, we arrive at:

$$\omega = \sqrt{\frac{(4k_b b + M(k_b + k_p) + 4Kb) - \sqrt{\begin{matrix}(-4k_b b - M(k_b + k_p) - 4Kb)^2 \\ -4(Mb)(4Kk_b + 4k_b k_p + 4Kk_p)\end{matrix}}}{2Mb}} \quad \text{(S98)}$$

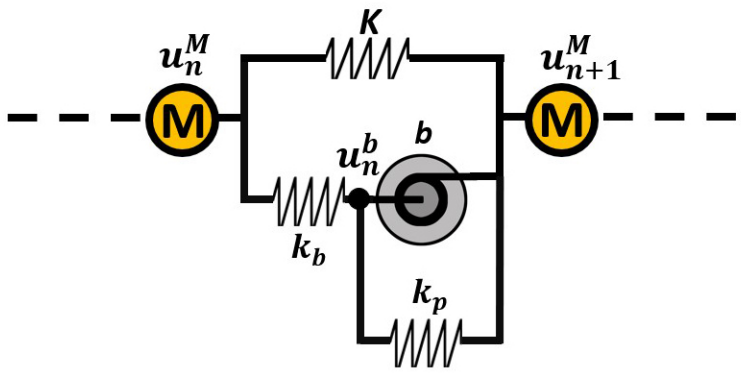

Figure S8: Unit cell with spring, k_p, in parallel to inerter.

Eq. (S98) can be normalized by $2\pi\sqrt{K/M}$:

$$f_{\mathrm{L}} = \frac{1}{2\pi}\sqrt{\frac{(4k_b b + M(k_b+k_p) + 4Kb) - \sqrt{\begin{matrix}(-4k_b b - M(k_b+k_p) - 4Kb)^2 \\ -4(Mb)(4Kk_b + 4k_b k_p + 4Kk_p)\end{matrix}}}{2Kb}} \tag{S99}$$

Taking $\mu_b = b/M$, $\kappa_b = k_b/K$ and $\kappa_p = k_p/K$, we get:

$$f_{\mathrm{L}} = \frac{1}{2\pi}\sqrt{\chi_p - \sqrt{\chi_p^2 - \frac{4(\kappa_b + \kappa_b\kappa_p + \kappa_p)}{\mu_b}}} \tag{S100}$$

where $\chi_p = 2\kappa_b + (\kappa_b + \kappa_p)/(2\mu_b) + 2$.

S7.2 Upper Edge of the Band Gap

Similarly, we can find the upper edge of the band gap at q=0, where Eqn. (S96) becomes:

$$-\omega^2 \begin{bmatrix} M+b & -b \\ -b & b \end{bmatrix} + \begin{bmatrix} k_b+k_p & -k_p-k_b \\ -k_b-k_p & k_b+k_p \end{bmatrix} = 0 \tag{S101}$$

Taking the larger eigen-frequency, we arrive at:

$$\omega = \sqrt{\frac{k_b+k_p}{b}} \tag{S102}$$

Eqn. (S102) can be normalized by $2\pi\sqrt{K/M}$:

$$f_{\mathrm{U}} = \frac{1}{2\pi}\sqrt{\frac{M(k_b+k_p)}{Kb}} \tag{S103}$$

Taking $\mu_b = b/M$, $\kappa_b = k_b/K$ and $\kappa_p = k_p/K$, we get:

$$f_{\mathrm{U}} = \frac{1}{2\pi}\sqrt{\frac{(\kappa_b+\kappa_p)}{\mu_b}} \tag{S104}$$

This is an important tunable parameter, k_p, has been included in the inerter-based metamaterial unit cell as shown in Fig. S8. Stiffness across the terminals of an inerter can have devastating effect on the band gap. As can be seen in Fig. S9, the presence of this stiffness not only increases the lower edge frequency but also destroys the bandgap by reducing the relative gap size. Hence, for the rest of the study k_p is taken as zero. However, it is noteworthy to consider that in practical case stiffness across inerter has the potential to form the bandgap lower than expected.

S7.3 Convergence Limit $\mu_b \gg \kappa_b$ and κ_p

Fig. S9 shows that as stiffness across inerter becomes large, the size of band gap diminishes with lower edge edge of the bang shift to higher frequency. For $\mu_b \gg \kappa_b$ and κ_p, Eqns. (S104) and (S100) becomes:

$$f_{\mathrm{U}} = \frac{\sqrt{\zeta_2}}{2\pi} \tag{S105}$$

where $\zeta_2 = (\kappa_b + \kappa_p)/\mu_b$.

$$(2\pi f_{\mathrm{L}})^2 = \chi_p' - \sqrt{{\chi_p'}^2 - 4\zeta_1} = \chi_p'\left(1 - \sqrt{1-\zeta_1'}\right) \tag{S106}$$

where $\chi_p' = 2\kappa_b + 2$, $\zeta_1 = (\kappa_b + \kappa_b\kappa_p + \kappa_p)/\mu_b$ and $\zeta_1' = 4\zeta_1/{\chi_p'}^2$
The first two terms of the Taylor series from Eqn. (S23) are significant. Hence, from the Eqns. (S106) and (S23) we arrive at:

$$(2\pi f_{\mathrm{L}})^2 \to \chi_p'\left(1 - \left(1 - \frac{\zeta_1'}{2}\right)\right) = \chi_p'\frac{\zeta_1'}{2} = \frac{2\zeta_1}{\chi_p'} \tag{S107}$$

$$f_{\mathrm{L}} \to \frac{1}{2\pi}\sqrt{\frac{2\zeta_1}{\chi_p'}} = \frac{1}{2\pi}\sqrt{\frac{\kappa_b}{\mu_b(\kappa_b+1)} + \frac{\kappa_p}{\mu_b}} \tag{S108}$$

Taking $\kappa_b = 1$, we arrive at:

$$f_{\mathrm{L}} \to \frac{1}{2\pi}\sqrt{\frac{2\kappa_p + 1}{2\mu_b}} \tag{S109}$$

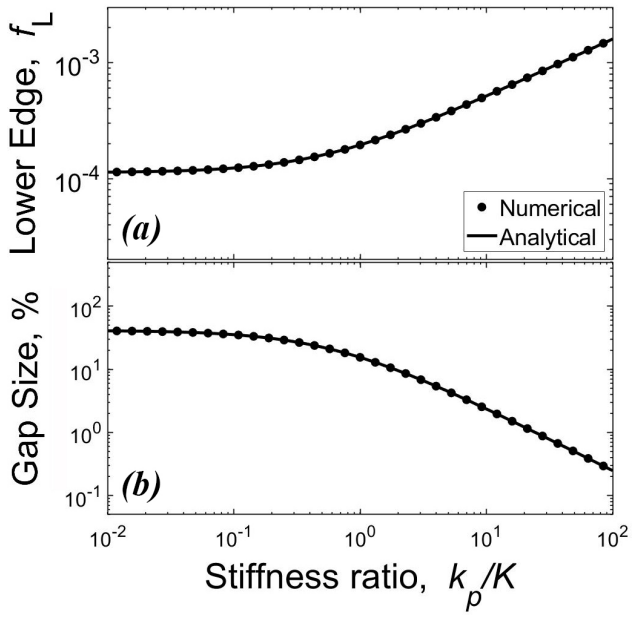

Figure S9: Here, $b = 10^6$ and $k_b = 1$ N/s. (a) Lower edge of the band gap. (b) relative size of the band gap.

For $\kappa_p = 1$ and $\mu_b = 10^6$, we get:

$$f_{\mathrm{L}} \approx 0.000195 \tag{S110}$$

For $\mu_b \gg \kappa_b$ and κ_p, the relative gap size converges to:

$$\Delta f = \frac{f_{\mathrm{U}} - f_{\mathrm{L}}}{f_{\mathrm{L}}} \to \frac{\sqrt{\zeta_2} - \sqrt{2\zeta_1/\chi'_p}}{\sqrt{2\zeta_1/\chi'_p}} = \sqrt{\frac{(\kappa_b + \kappa_p)(\kappa_b + 1)}{\kappa_b + \kappa_b\kappa_p + \kappa_p}} - 1 \tag{S111}$$

Taking $\kappa_b = 1$, we arrive at:

$$\Delta f \to \sqrt{\frac{2(\kappa_p + 1)}{2\kappa_p + 1}} - 1 = \sqrt{1 + \frac{1}{2\kappa_p + 1}} - 1. \tag{S112}$$

For $\kappa_p = 1$ and $\mu_b = 10^6$, we get at:

$$\Delta f \approx 15.5\% \tag{S113}$$

S8 Square Lattice Formulation and Results

Real space and reciprocal lattice primitive vectors for square lattice with lattice constant a (shown in Fig. S10(a) and (b), respectively) are defined as [7]:

$$\begin{aligned} \boldsymbol{a_1} &= a\hat{\boldsymbol{x}} \\ \boldsymbol{a_2} &= a\hat{\boldsymbol{y}} \\ \boldsymbol{b_1} &= \frac{2\pi}{a}\hat{\boldsymbol{x}} \\ \boldsymbol{b_2} &= \frac{2\pi}{a}\hat{\boldsymbol{y}} \end{aligned} \tag{S114}$$

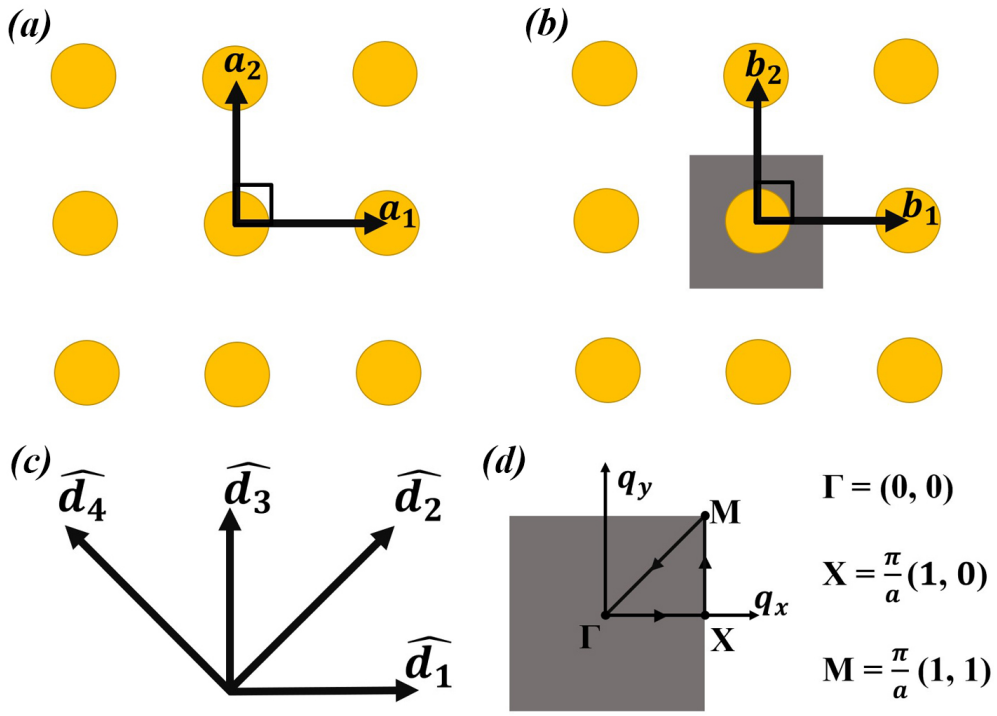

Figure S10: (a) Unit cell of square lattice in real space. (b) Reciprocal lattice in the reciprocal space and Brillouin zone (gray region) of the corresponding square lattice. (c) $\hat{d}_1$, $\hat{d}_2$, $\hat{d}_3$ and $\hat{d}_4$ are unit vectors associated to the directions of the springs and inerters. (d) Irreducible Brillouin zone (shaded gray square) for the square lattice. The dispersion relation is plotted for wave vectors q along the direction determined by the $M - \Gamma - X$ points.

Taking d as the vector at the end points of unstrained springs, direction unit vectors as shown in Fig. S10(c) can be defined as [9]:

$$\begin{aligned}
\hat{\boldsymbol{d}}_1 &= \frac{\boldsymbol{d_1}}{|\boldsymbol{d_1}|} = \begin{pmatrix}\cos 0\\ \sin 0\end{pmatrix} = \begin{pmatrix}1\\ 0\end{pmatrix}\\
\hat{\boldsymbol{d}}_2 &= \frac{\boldsymbol{d_2}}{|\boldsymbol{d_2}|} = \begin{pmatrix}\cos 45\\ \sin 45\end{pmatrix} = \begin{pmatrix}\frac{1}{\sqrt{2}}\\ \frac{1}{\sqrt{2}}\end{pmatrix}\\
\hat{\boldsymbol{d}}_3 &= \frac{\boldsymbol{d_3}}{|\boldsymbol{d_3}|} = \begin{pmatrix}\cos 90\\ \sin 90\end{pmatrix} = \begin{pmatrix}0\\ 1\end{pmatrix}\\
\hat{\boldsymbol{d}}_4 &= \frac{\boldsymbol{d_4}}{|\boldsymbol{d_4}|} = \begin{pmatrix}\cos 135\\ \sin 135\end{pmatrix} = \begin{pmatrix}-\frac{1}{\sqrt{2}}\\ \frac{1}{\sqrt{2}}\end{pmatrix}
\end{aligned} \tag{S115}$$

Degrees of freedom in inerter-based square lattice are:

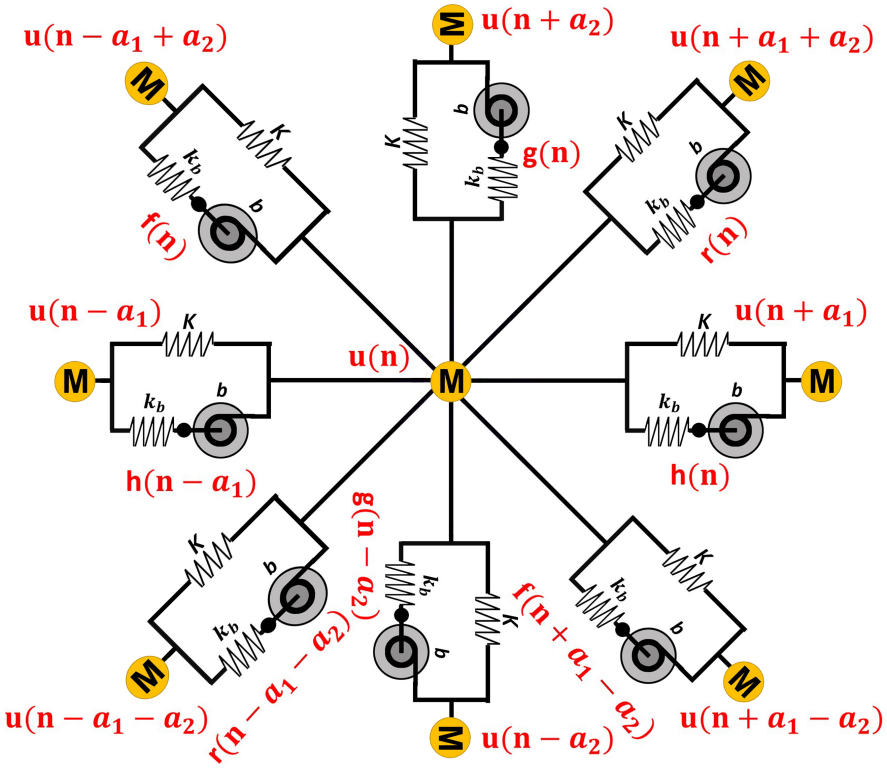

Figure S11: Degrees of freedom in Square lattice.

$$
\begin{aligned}
\boldsymbol{u}(\boldsymbol{n}) &= \begin{pmatrix} u_x(\boldsymbol{n}) \\ u_y(\boldsymbol{n}) \end{pmatrix} \\
\boldsymbol{h}(\boldsymbol{n}) &= \begin{pmatrix} h_x(\boldsymbol{n}) \\ h_y(\boldsymbol{n}) \end{pmatrix} \\
\boldsymbol{g}(\boldsymbol{n}) &= \begin{pmatrix} g_x(\boldsymbol{n}) \\ g_y(\boldsymbol{n}) \end{pmatrix} \\
\boldsymbol{r}(\boldsymbol{n}) &= \begin{pmatrix} r_x(\boldsymbol{n}) \\ r_y(\boldsymbol{n}) \end{pmatrix} \\
\boldsymbol{f}(\boldsymbol{n}) &= \begin{pmatrix} f_x(\boldsymbol{n}) \\ f_y(\boldsymbol{n}) \end{pmatrix}
\end{aligned}
\tag{S116}
$$

where

$$
\boldsymbol{n} = \begin{pmatrix} n_x \\ n_y \end{pmatrix}. \tag{S117}
$$

Here, $\boldsymbol{u}(\boldsymbol{n})$ is the displacement on the main chain of unit cell at position vector $\boldsymbol{n}$ with mass M and stiffness K in the directions $\hat{\boldsymbol{d}}_{\boldsymbol{1}}$, $\hat{\boldsymbol{d}}_{\boldsymbol{2}}$, $\hat{\boldsymbol{d}}_{\boldsymbol{3}}$ and $\hat{\boldsymbol{d}}_{\boldsymbol{4}}$; $\boldsymbol{h}(\boldsymbol{n})$, $\boldsymbol{g}(\boldsymbol{n})$, $\boldsymbol{r}(\boldsymbol{n})$ and $\boldsymbol{f}(\boldsymbol{n})$ are degrees of freedom at $\boldsymbol{n}^{th}$ cell between the inerter with inertance b and the spring with stiffness k_b in the directions $\hat{\boldsymbol{d}}_{\boldsymbol{1}}$, $\hat{\boldsymbol{d}}_{\boldsymbol{3}}$, $\hat{\boldsymbol{d}}_{\boldsymbol{2}}$ and $\hat{\boldsymbol{d}}_{\boldsymbol{4}}$, respectively.

Newton's equation of motion:

$$
\begin{aligned}
&M\ddot{\boldsymbol{u}}(\boldsymbol{n}) + K\ \hat{\boldsymbol{d}}_{\boldsymbol{1}} \otimes \hat{\boldsymbol{d}}_{\boldsymbol{1}}(\boldsymbol{u}(\boldsymbol{n}) + \boldsymbol{u}(\boldsymbol{n}+\boldsymbol{a}_{\boldsymbol{1}}) + K\ \hat{\boldsymbol{d}}_{\boldsymbol{1}} \otimes \hat{\boldsymbol{d}}_{\boldsymbol{1}}(\boldsymbol{u}(\boldsymbol{n}) + \boldsymbol{u}(\boldsymbol{n}-\boldsymbol{a}_{\boldsymbol{1}})) \\
&+K\ \hat{\boldsymbol{d}}_{\boldsymbol{2}} \otimes \hat{\boldsymbol{d}}_{\boldsymbol{2}}(\boldsymbol{u}(\boldsymbol{n}) - \boldsymbol{u}(\boldsymbol{n}+\boldsymbol{a}_{\boldsymbol{1}}+\boldsymbol{a}_{\boldsymbol{2}}) + K\ \hat{\boldsymbol{d}}_{\boldsymbol{2}} \otimes \hat{\boldsymbol{d}}_{\boldsymbol{2}}(\boldsymbol{u}(\boldsymbol{n}) - \boldsymbol{u}(\boldsymbol{n}-\boldsymbol{a}_{\boldsymbol{1}}-\boldsymbol{a}_{\boldsymbol{2}}) \\
&+K\ \hat{\boldsymbol{d}}_{\boldsymbol{3}} \otimes \hat{\boldsymbol{d}}_{\boldsymbol{3}}(\boldsymbol{u}(\boldsymbol{n}) - \boldsymbol{u}(\boldsymbol{n}+\boldsymbol{a}_{\boldsymbol{2}}) + K\ \hat{\boldsymbol{d}}_{\boldsymbol{3}} \otimes \hat{\boldsymbol{d}}_{\boldsymbol{3}}(\boldsymbol{u}(\boldsymbol{n}) - \boldsymbol{u}(\boldsymbol{n}-\boldsymbol{a}_{\boldsymbol{2}}) \\
&+K\ \hat{\boldsymbol{d}}_{\boldsymbol{4}} \otimes \hat{\boldsymbol{d}}_{\boldsymbol{4}}(\boldsymbol{u}(\boldsymbol{n}) - \boldsymbol{u}(\boldsymbol{n}-\boldsymbol{a}_{\boldsymbol{1}}+\boldsymbol{a}_{\boldsymbol{2}}) + K\ \hat{\boldsymbol{d}}_{\boldsymbol{4}} \otimes \hat{\boldsymbol{d}}_{\boldsymbol{4}}(\boldsymbol{u}(\boldsymbol{n}) - \boldsymbol{u}(\boldsymbol{n}+\boldsymbol{a}_{\boldsymbol{1}}-\boldsymbol{a}_{\boldsymbol{2}}) \\
&+k_b\ \hat{\boldsymbol{d}}_{\boldsymbol{1}} \otimes \hat{\boldsymbol{d}}_{\boldsymbol{1}}(\boldsymbol{u}(\boldsymbol{n}) - \boldsymbol{h}(\boldsymbol{n})) + b\ \hat{\boldsymbol{d}}_{\boldsymbol{1}} \otimes \hat{\boldsymbol{d}}_{\boldsymbol{1}}(\boldsymbol{u}(\boldsymbol{n}) - \boldsymbol{h}(\boldsymbol{n}-\boldsymbol{a}_{\boldsymbol{1}})) \\
&+k_b\ \hat{\boldsymbol{d}}_{\boldsymbol{2}} \otimes \hat{\boldsymbol{d}}_{\boldsymbol{2}}(\boldsymbol{u}(\boldsymbol{n}) - \boldsymbol{r}(\boldsymbol{n})) + b\ \hat{\boldsymbol{d}}_{\boldsymbol{2}} \otimes \hat{\boldsymbol{d}}_{\boldsymbol{2}}(\boldsymbol{u}(\boldsymbol{n}) - \boldsymbol{r}(\boldsymbol{n}-\boldsymbol{a}_{\boldsymbol{1}}-\boldsymbol{a}_{\boldsymbol{2}}) \\
&+k_b\ \hat{\boldsymbol{d}}_{\boldsymbol{3}} \otimes \hat{\boldsymbol{d}}_{\boldsymbol{3}}(\boldsymbol{u}(\boldsymbol{n}) - \boldsymbol{g}(\boldsymbol{n})) + b\ \hat{\boldsymbol{d}}_{\boldsymbol{3}} \otimes \hat{\boldsymbol{d}}_{\boldsymbol{3}}(\boldsymbol{u}(\boldsymbol{n}) - \boldsymbol{g}(\boldsymbol{n}-\boldsymbol{a}_{\boldsymbol{2}})) \\
&+k_b\ \hat{\boldsymbol{d}}_{\boldsymbol{4}} \otimes \hat{\boldsymbol{d}}_{\boldsymbol{4}}(\boldsymbol{u}(\boldsymbol{n}) - \boldsymbol{f}(\boldsymbol{n})) + b\ \hat{\boldsymbol{d}}_{\boldsymbol{4}} \otimes \hat{\boldsymbol{d}}_{\boldsymbol{4}}(\boldsymbol{u}(\boldsymbol{n}) - \boldsymbol{f}(\boldsymbol{n}+\boldsymbol{a}_{\boldsymbol{1}}-\boldsymbol{a}_{\boldsymbol{2}}))
\end{aligned}
= 0 \tag{S118}
$$

$$
k_b\ \hat{\boldsymbol{d}}_{\boldsymbol{1}} \otimes \hat{\boldsymbol{d}}_{\boldsymbol{1}}(\boldsymbol{h}(\boldsymbol{n}) - \boldsymbol{u}(\boldsymbol{n})) + b\ \hat{\boldsymbol{d}}_{\boldsymbol{1}} \otimes \hat{\boldsymbol{d}}_{\boldsymbol{1}}(\ddot{\boldsymbol{h}}(\boldsymbol{n}) - \ddot{\boldsymbol{u}}(\boldsymbol{n}+\boldsymbol{a}_{\boldsymbol{1}})) = 0 \tag{S119}
$$

$$
k_b\ \hat{\boldsymbol{d}}_{\boldsymbol{2}} \otimes \hat{\boldsymbol{d}}_{\boldsymbol{2}}(\boldsymbol{r}(\boldsymbol{n}) - \boldsymbol{u}(\boldsymbol{n})) + b\ \hat{\boldsymbol{d}}_{\boldsymbol{2}} \otimes \hat{\boldsymbol{d}}_{\boldsymbol{2}}(\ddot{\boldsymbol{r}}(\boldsymbol{n}) - \ddot{\boldsymbol{u}}(\boldsymbol{n}+\boldsymbol{a}_{\boldsymbol{1}}+\boldsymbol{a}_{\boldsymbol{2}})) = 0 \tag{S120}
$$

$$
k_b\ \hat{\boldsymbol{d}}_{\boldsymbol{3}} \otimes \hat{\boldsymbol{d}}_{\boldsymbol{3}}(\boldsymbol{g}(\boldsymbol{n}) - \boldsymbol{u}(\boldsymbol{n})) + b\ \hat{\boldsymbol{d}}_{\boldsymbol{3}} \otimes \hat{\boldsymbol{d}}_{\boldsymbol{3}}(\ddot{\boldsymbol{g}}(\boldsymbol{n}) - \ddot{\boldsymbol{u}}(\boldsymbol{n}+\boldsymbol{a}_{\boldsymbol{2}})) = 0 \tag{S121}
$$

$$
k_b\ \hat{\boldsymbol{d}}_{\boldsymbol{4}} \otimes \hat{\boldsymbol{d}}_{\boldsymbol{4}}(\boldsymbol{f}(\boldsymbol{n}) - \boldsymbol{u}(\boldsymbol{n})) + b\ \hat{\boldsymbol{d}}_{\boldsymbol{4}} \otimes \hat{\boldsymbol{d}}_{\boldsymbol{4}}(\ddot{\boldsymbol{f}}(\boldsymbol{n}) - \ddot{\boldsymbol{u}}(\boldsymbol{n}-\boldsymbol{a}_{\boldsymbol{1}}+\boldsymbol{a}_{\boldsymbol{2}})) = 0 \tag{S122}
$$

From Eqns. (S114), (S115), (S116), (S118), (S119), (S120), (S121) and (S122),

$$
\begin{aligned}
M\ddot{u}_x(0,0) + K(u_x(0,0) - u_x(-1,0) + K(u_x(0,0) - u_x(1,0) \\
+k_b(u_x(0,0) - h_x(0,0)) + b(\ddot{u}_x(0,0) - \ddot{h}_x(-1,0)) \\
+\frac{K}{2}(u_x(0,0) - u_x(1,1)) + \frac{K}{2}(u_x(0,0) - u_x(-1,1)) \\
+\frac{K}{2}(u_x(0,0) - u_x(-1,-1)) + \frac{K}{2}(u_x(0,0) - u_x(1,-1)) \\
+\frac{K}{2}(u_y(0,0) - u_y(1,1)) - \frac{K}{2}(u_y(0,0) - u_y(-1,1)) \\
+\frac{K}{2}(u_y(0,0) - u_y(-1,-1)) - \frac{K}{2}(u_y(0,0) - u_y(1,-1)) = 0
\end{aligned} \tag{S123}
$$

$$
\begin{aligned}
+\frac{k_b}{2}(u_x(0,0) - r_x(0,0)) + \frac{b}{2}(\ddot{u}_x(0,0) - \ddot{r}_x(-1,-1)) \\
+\frac{k_b}{2}(u_x(0,0) - f_x(0,0)) + \frac{b}{2}(\ddot{u}_x(0,0) - \ddot{f}_x(1,-1)) \\
+\frac{k_b}{2}(u_y(0,0) - r_y(0,0)) + \frac{b}{2}(\ddot{u}_y(0,0) - \ddot{r}_y(-1,-1)) \\
-\frac{k_b}{2}(u_y(0,0) - f_y(0,0)) - \frac{b}{2}(\ddot{u}_y(0,0) - \ddot{f}_y(1,-1))
\end{aligned}
$$

$$
\begin{aligned}
M\ddot{u}_y(0,0) + K(u_y(0,0) - u_y(0,-1)) + K(u_y(0,0) - u_y(0,1)) \\
+k_b(u_y(0,0) - g_y(0,0)) + b(\ddot{u}_y(0,0) - \ddot{g}_y(0,-1)) \\
+\frac{K}{2}(u_y(0,0) - u_y(1,1) + \frac{K}{2}(u_y(0,0) - u_y(-1,1) \\
+\frac{K}{2}(u_y(0,0) - u_y(-1,-1) + \frac{K}{2}(u_y(0,0) - u_y(1,-1) \\
+\frac{K}{2}(u_x(0,0) - u_x(1,1) - \frac{K}{2}(u_x(0,0) - u_x(-1,1) \\
+\frac{K}{2}(u_x(0,0) - u_x(-1,-1) - \frac{K}{2}(u_x(0,0) - u_x(1,-1) = 0
\end{aligned} \tag{S124}
$$

$$
\begin{aligned}
+\frac{k_b}{2}(u_y(0,0) - r_y(0,0)) + \frac{b}{2}(\ddot{u}_y(0,0) - \ddot{r}_y(-1,-1)) \\
+\frac{k_b}{2}(u_y(0,0) - f_y(0,0)) + \frac{b}{2}(\ddot{u}_y(0,0) - \ddot{f}_y(1,-1)) \\
+\frac{k_b}{2}(u_x(0,0) - r_x(0,0)) + \frac{b}{2}(\ddot{u}_x(0,0) - \ddot{r}_x(-1,-1)) \\
-\frac{k_b}{2}(u_x(0,0) - f_x(0,0)) - \frac{b}{2}(\ddot{u}_x(0,0) - \ddot{f}_x(+1,-1))
\end{aligned}
$$

$$
k_b(h_x(0,0) - u_x(0,0)) + b(\ddot{h}_x(0,0) - \ddot{u}_x(1,0) = 0 \tag{S125}
$$

$$
k_b(g_y(0,0) - u_y(0,0)) + b(\ddot{g}_y(0,0) - \ddot{u}_y(0,1) = 0 \tag{S126}
$$

$$
\begin{aligned}
\frac{k_b}{2}(r_x(0,0) - u_x(0,0)) + \frac{b}{2}(\ddot{r}_x(0,0) - \ddot{u}_x(1,1)) \\
+\frac{k_b}{2}(r_y(0,0) - u_y(0,0)) + \frac{b}{2}(\ddot{r}_y(0,0) - \ddot{u}_y(1,1))
\end{aligned} = 0 \tag{S127}
$$

$$\begin{aligned}\frac{k_b}{2}(r_y(0,0)-u_y(0,0))+\frac{b}{2}(\ddot{r}_y(0,0)-\ddot{u}_y(1,1))\\ +\frac{k_b}{2}(r_x(0,0)-u_x(0,0))+\frac{b}{2}(\ddot{r}_x(0,0)-\ddot{u}_x(1,1))\end{aligned}=0 \tag{S128}$$

$$\begin{aligned}\frac{k_b}{2}(f_x(0,0)-u_x(0,0))+\frac{b}{2}(\ddot{f}_x(0,0)-\ddot{u}_x(-1,1))\\ -\frac{k_b}{2}(f_y(0,0)-u_y(0,0))-\frac{b}{2}(\ddot{f}_y(0,0)-\ddot{u}_y(-1,1))\end{aligned}=0 \tag{S129}$$

$$\begin{aligned}\frac{k_b}{2}(f_y(0,0)-u_y(0,0))+\frac{b}{2}(\ddot{f}_y(0,0)-\ddot{u}_y(-1,1))\\ -\frac{k_b}{2}(f_x(0,0)-u_x(0,0))-\frac{b}{2}(\ddot{f}_x(0,0)-\ddot{u}_x(-1,1))\end{aligned}=0 \tag{S130}$$

The components of degrees of freedom in Eqn. (S116) are define according to the Bloch theorem [5],

$$u_x(\boldsymbol{n}) = U_x e^{n_x a q_x + n_y a q_y + i\omega t} \tag{S131}$$

$$u_y(\boldsymbol{n}) = U_y e^{n_x a q_x + n_y a q_y + i\omega t} \tag{S132}$$

$$h_x(\boldsymbol{n}) = H_x e^{n_x a q_x + n_y a q_y + i\omega t} \tag{S133}$$

$$g_y(\boldsymbol{n}) = G_y e^{n_x a q_x + n_y a q_y + i\omega t} \tag{S134}$$

$$r_x(\boldsymbol{n}) = R_x e^{n_x a q_x + n_y a q_y + i\omega t} \tag{S135}$$

$$r_y(\boldsymbol{n}) = R_y e^{n_x a q_x + n_y a q_y + i\omega t} \tag{S136}$$

$$f_x(\boldsymbol{n}) = F_x e^{n_x a q_x + n_y a q_y + i\omega t} \tag{S137}$$

$$f_y(\boldsymbol{n}) = F_y e^{n_x a q_x + n_y a q_y + i\omega t} \tag{S138}$$

where q_x and q_y are wave vectors in the reciprocal space in x and y directions, respectively. Substituting Eqns. (S131), (S132), (S133), (S134), (S135), (S136), (S137) and (S138) into the the Eqns. (S123), (S124), (S125), (S126), (S127), (S128), (S129) and (S130), we get

$$-\omega^2[M]+[K]=0 \tag{S139}$$

where M is mass operator and K is stiffness operator as follows

$$[K]=\begin{bmatrix}
\alpha_{1,1}+2k_b & \alpha_{1,2} & -k_b & 0 & -\frac{k_b}{2} & -\frac{k_b}{2} & -\frac{k_b}{2} & \frac{k_b}{2}\\
\alpha_{2,1} & \alpha_{2,2}+2k_b & 0 & -k_b & -\frac{k_b}{2} & -\frac{k_b}{2} & \frac{k_b}{2} & -\frac{k_b}{2}\\
-k_b & 0 & k_b & 0 & 0 & 0 & 0 & 0\\
0 & -k_b & 0 & k_b & 0 & 0 & 0 & 0\\
-\frac{k_b}{2} & -\frac{k_b}{2} & 0 & 0 & \frac{k_b}{2} & \frac{k_b}{2} & 0 & 0\\
-\frac{k_b}{2} & -\frac{k_b}{2} & 0 & 0 & \frac{k_b}{2} & \frac{k_b}{2} & 0 & 0\\
-\frac{k_b}{2} & \frac{k_b}{2} & 0 & 0 & 0 & 0 & \frac{k_b}{2} & -\frac{k_b}{2}\\
\frac{k_b}{2} & -\frac{k_b}{2} & 0 & 0 & 0 & 0 & -\frac{k_b}{2} & \frac{k_b}{2}
\end{bmatrix} \tag{S140}$$

$$[M] = \begin{bmatrix} M+2b & 0 & -be^{-q_x} & 0 & -\frac{b}{2}\beta_3 & -\frac{b}{2}\beta_3 & -\frac{b}{2}\beta_4 & \frac{b}{2}\beta_4 \\ 0 & M+2b & 0 & -b & -\frac{b}{2}\beta_3 & -\frac{b}{2}\beta_3 & \frac{b}{2}\beta_4 & -\frac{b}{2}\beta_4 \\ -be^{q_x} & 0 & b & 0 & 0 & 0 & 0 & 0 \\ 0 & -be^{q_y} & 0 & b & 0 & 0 & 0 & 0 \\ -\frac{b}{2}\beta_1 & -\frac{b}{2}\beta_1 & 0 & 0 & \frac{b}{2} & \frac{b}{2} & 0 & 0 \\ -\frac{b}{2}\beta_1 & -\frac{b}{2}\beta_1 & 0 & 0 & \frac{b}{2} & \frac{b}{2} & 0 & 0 \\ -\frac{b}{2}\beta_2 & \frac{b}{2}\beta_2 & 0 & 0 & 0 & 0 & \frac{b}{2} & -\frac{b}{2} \\ \frac{b}{2}\beta_2 & -\frac{b}{2}\beta_2 & 0 & 0 & 0 & 0 & -\frac{b}{2} & \frac{b}{2} \end{bmatrix} \tag{S141}$$

where,

$$\begin{aligned} \alpha_{1,1} &= 2K - Ke^{q_x} - Ke^{-q_x} + \frac{K}{2}(4 - \beta_1 - \beta_2 - \beta_3 - \beta_4) \\ \alpha_{1,2} &= \frac{K}{2}(-\beta_1 + \beta_2 - \beta_3 + \beta_4) \\ \alpha_{2,1} &= \frac{K}{2}(-\beta_1 + \beta_2 - \beta_3 + \beta_4) \\ \alpha_{2,2} &= 2K - Ke^{q_y} - Ke^{-q_y} + \frac{K}{2}(4 - \beta_1 - \beta_2 - \beta_3 - \beta_4) \\ \beta_1 &= e^{q_x+q_y} \\ \beta_2 &= e^{-q_x+q_y} \\ \beta_3 &= e^{-q_x-q_y} \\ \beta_4 &= e^{q_x-q_y} \end{aligned} \tag{S142}$$

The degrees of freedom in h_y and g_x have been constrained as can be seen. The following matrix operation on both M and K operators will constrain two more degrees of freedoms.

$$\begin{aligned} K_{C7} &\longrightarrow K_{C_7} - K_{C_8} \\ K_{C8} &\longrightarrow 0_{8\times 1} \\ K_{R7} &\longrightarrow K_{R_7} - K_{R_8} \\ K_{R8} &\longrightarrow 0_{1\times 8} \\ K_{C5} &\longrightarrow K_{C5} + K_{C6} \\ K_{C6} &\longrightarrow 0_{8\times 1} \\ K_{R5} &\longrightarrow K_{R5} + K_{R6} \\ K_{R6} &\longrightarrow 0_{1\times 8} \end{aligned} \tag{S143}$$

$$\begin{aligned} M_{C7} &\longrightarrow M_{C_7} - M_{C_8} \\ M_{C8} &\longrightarrow 0_{8\times 1} \\ M_{R7} &\longrightarrow M_{R_7} - M_{R_8} \\ M_{R8} &\longrightarrow 0_{1\times 8} \\ M_{C5} &\longrightarrow M_{C5} + M_{C6} \\ M_{C6} &\longrightarrow 0_{8\times 1} \\ M_{R5} &\longrightarrow M_{R5} + M_{R6} \\ M_{R6} &\longrightarrow 0_{1\times 8} \end{aligned} \tag{S144}$$

This will result in a 6×6 M and K operators. Solving for eigenvalue problem will give the results.

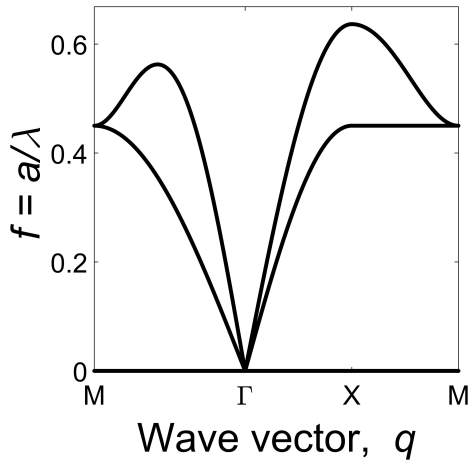

Figure S12: Band structure of inerter-based square lattice.

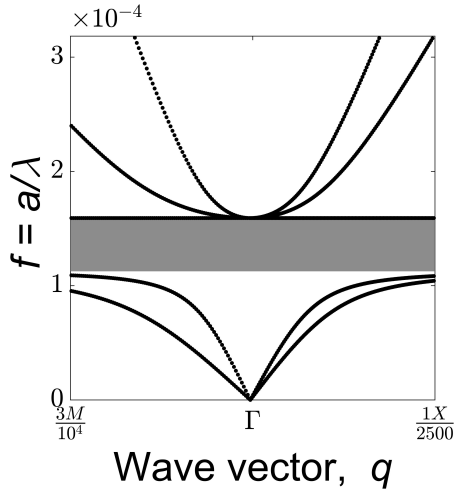

Figure S13: Zoomed version of Fig. S12 showing the band gap.

Fig. S12 and Fig. S13 shows the band structure for wave travelling in direction $M-\Gamma-X-M$. Fig. S14 and Fig. S15 shows the band structure in all directions of q_x and q_y.

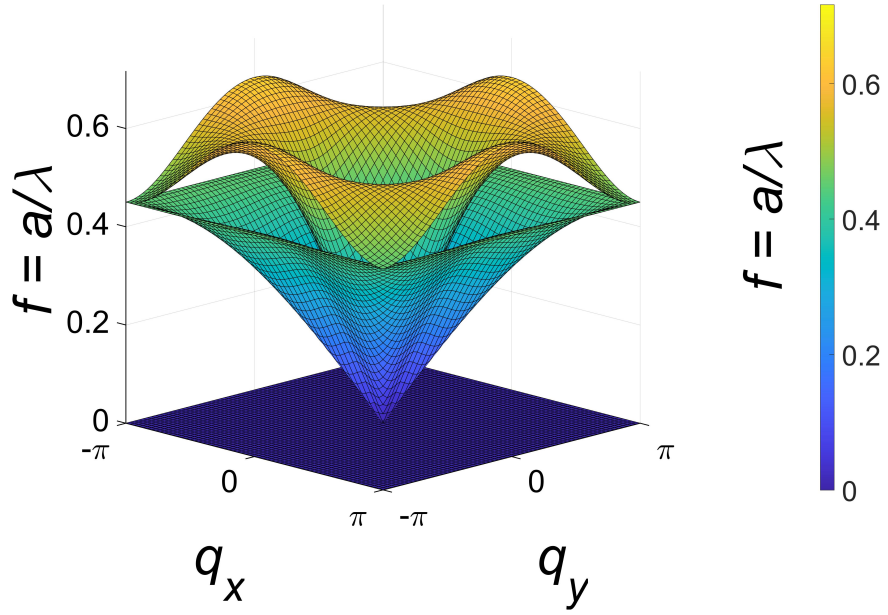

Figure S14: Full band structure for inerter based square lattice.

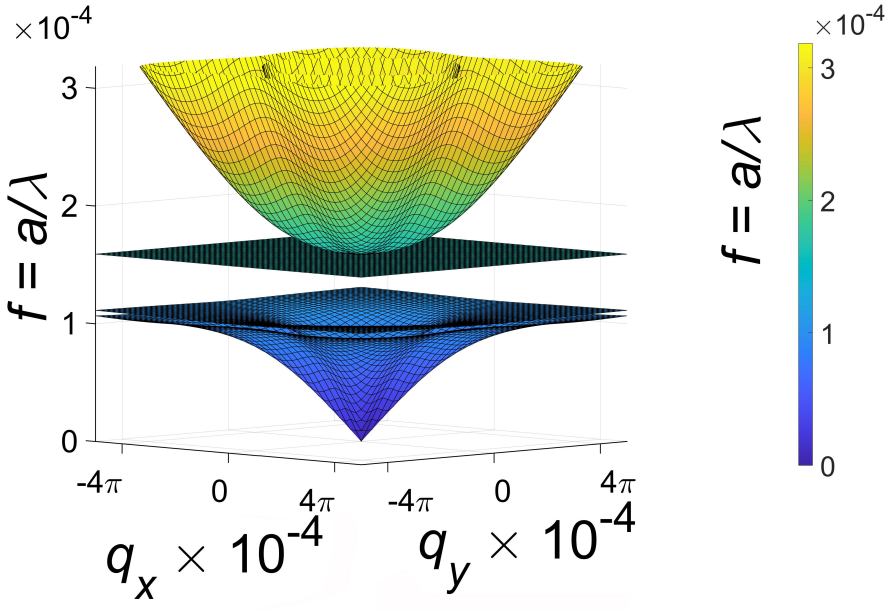

Figure S15: Zoomed band structure for inerter based square lattice showing the bandgap.

S9 Triangular Lattice Formulation and Results

Real space and reciprocal lattice primitive vectors for triangular lattice with lattice constant a (shown in Fig. S16(a) and (b), respectively) are defined as [7]:

$$\begin{aligned}
\boldsymbol{a_1} &= a\hat{\boldsymbol{x}} \\
\boldsymbol{a_2} &= \frac{a}{2}\hat{\boldsymbol{x}} + \frac{\sqrt{3}a}{2}\hat{\boldsymbol{y}} \\
\boldsymbol{b_1} &= \frac{4\pi}{\sqrt{3}a}\left(\frac{\sqrt{3}}{2}\hat{\boldsymbol{x}} - \frac{1}{2}\hat{\boldsymbol{y}}\right) \\
\boldsymbol{b_2} &= \frac{4\pi}{\sqrt{3}a}\hat{\boldsymbol{y}}
\end{aligned} \tag{S145}$$

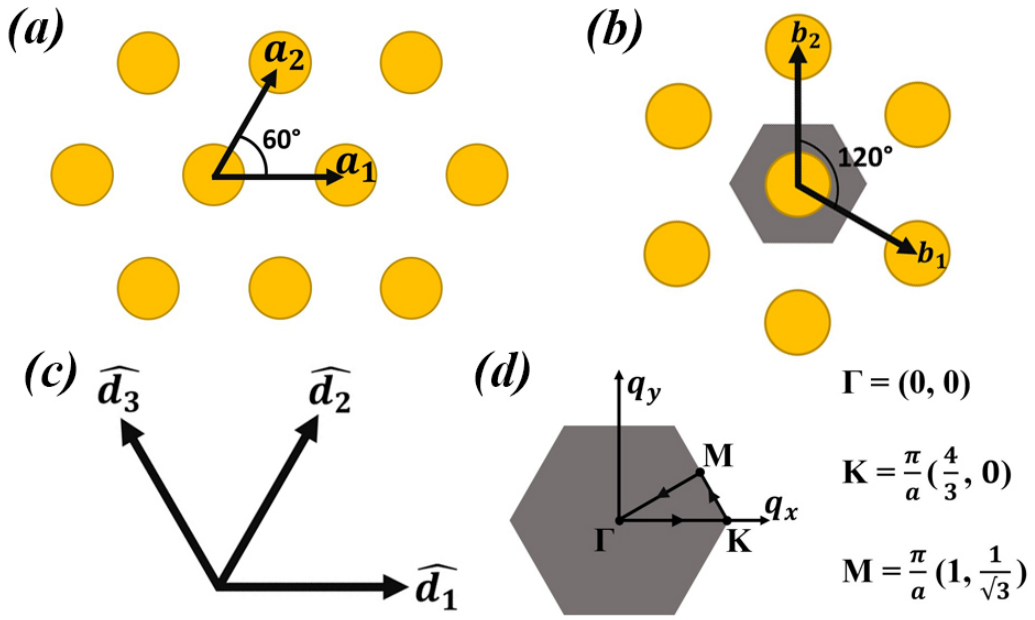

Figure S16: (a) Unit cell of triangular lattice in real space. (b) Reciprocal lattice in the reciprocal space and Brillouin zone (gray region) of the corresponding triangular lattice. (c) $\hat{d}_1$, $\hat{d}_2$ and $\hat{d}_3$ are unit vectors associated to the directions of the springs and inerters. (d) Irreducible Brillouin zone (shaded gray hexagon) for the triangular lattice. The dispersion relation is plotted for wave vectors q along the direction determined by the $\Gamma - K - M$ points.

Taking $\boldsymbol{d}$ as the vector at the end points of unstrained springs, direction unit vectors as shown in Fig. S16(c) can be defined as [9]:

$$\begin{aligned}
\hat{\boldsymbol{d}}_1 &= \frac{\boldsymbol{d_1}}{|\boldsymbol{d_1}|} = \begin{pmatrix} \cos 0 \\ \sin 0 \end{pmatrix} = \begin{pmatrix} 1 \\ 0 \end{pmatrix} \\
\hat{\boldsymbol{d}}_2 &= \frac{\boldsymbol{d_2}}{|\boldsymbol{d_2}|} = \begin{pmatrix} \cos 60 \\ \sin 60 \end{pmatrix} = \begin{pmatrix} \frac{1}{2} \\ \frac{\sqrt{3}}{2} \end{pmatrix} \\
\hat{\boldsymbol{d}}_3 &= \frac{\boldsymbol{d_3}}{|\boldsymbol{d_3}|} = \begin{pmatrix} \cos 120 \\ \sin 120 \end{pmatrix} = \begin{pmatrix} -\frac{1}{2} \\ \frac{\sqrt{3}}{2} \end{pmatrix}
\end{aligned} \tag{S146}$$

Degrees of freedom in inerter-based triangular lattice are:

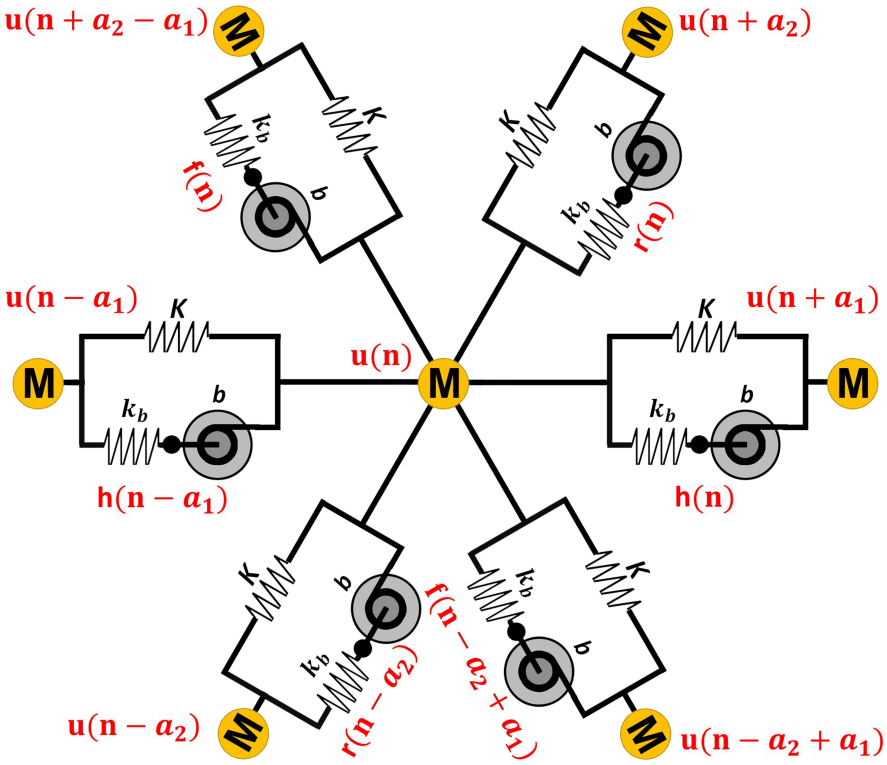

Figure S17: Degrees of freedom in triangular lattice.

$$\begin{aligned}
\boldsymbol{u}(\boldsymbol{n}) &= \begin{pmatrix} u_x(\boldsymbol{n}) \\ u_y(\boldsymbol{n}) \end{pmatrix} \\
\boldsymbol{h}(\boldsymbol{n}) &= \begin{pmatrix} h_x(\boldsymbol{n}) \\ h_y(\boldsymbol{n}) \end{pmatrix} \\
\boldsymbol{r}(\boldsymbol{n}) &= \begin{pmatrix} r_x(\boldsymbol{n}) \\ r_y(\boldsymbol{n}) \end{pmatrix} \\
\boldsymbol{f}(\boldsymbol{n}) &= \begin{pmatrix} f_x(\boldsymbol{n}) \\ f_y(\boldsymbol{n}) \end{pmatrix}
\end{aligned} \tag{S147}$$

where,

$$\boldsymbol{n} = \begin{pmatrix} n_x \\ n_y \end{pmatrix} \tag{S148}$$

Here, $\boldsymbol{u}(\boldsymbol{n})$ is the displacement on the main chain of unit cell at position vector $\boldsymbol{n}$ with mass M and stiffness K in the directions $\hat{\boldsymbol{d}}_{\boldsymbol{1}}$, $\hat{\boldsymbol{d}}_{\boldsymbol{2}}$ and $\hat{\boldsymbol{d}}_{\boldsymbol{3}}$; $\boldsymbol{h}(\boldsymbol{n})$, $\boldsymbol{r}(\boldsymbol{n})$ and $\boldsymbol{f}(\boldsymbol{n})$ are degrees of freedom at $\boldsymbol{n}^{th}$ cell between the inerter with inertance b and the spring with stiffness k_b in the directions $\hat{\boldsymbol{d}}_{\boldsymbol{1}}$, $\hat{\boldsymbol{d}}_{\boldsymbol{2}}$ and $\hat{\boldsymbol{d}}_{\boldsymbol{3}}$, respectively.

Newton's equation of motion:

$$\begin{aligned}
&M\ddot{\boldsymbol{u}}(\boldsymbol{n}) + K\ \hat{\boldsymbol{d}}_{\boldsymbol{1}} \otimes \hat{\boldsymbol{d}}_{\boldsymbol{1}}(\boldsymbol{u}(\boldsymbol{n}) - \boldsymbol{u}(\boldsymbol{n}+\boldsymbol{a}_{\boldsymbol{1}}) + K\ \hat{\boldsymbol{d}}_{\boldsymbol{1}} \otimes \hat{\boldsymbol{d}}_{\boldsymbol{1}}(\boldsymbol{u}(\boldsymbol{n}) - \boldsymbol{u}(\boldsymbol{n}-\boldsymbol{a}_{\boldsymbol{1}})) \\
&\quad + K\ \hat{\boldsymbol{d}}_{\boldsymbol{2}} \otimes \hat{\boldsymbol{d}}_{\boldsymbol{2}}(\boldsymbol{u}(\boldsymbol{n}) - \boldsymbol{u}(\boldsymbol{n}+\boldsymbol{a}_{\boldsymbol{2}}) + K\ \hat{\boldsymbol{d}}_{\boldsymbol{2}} \otimes \hat{\boldsymbol{d}}_{\boldsymbol{2}}(\boldsymbol{u}(\boldsymbol{n}) - \boldsymbol{u}(\boldsymbol{n}-\boldsymbol{a}_{\boldsymbol{2}}) \\
&+ K\ \hat{\boldsymbol{d}}_{\boldsymbol{3}} \otimes \hat{\boldsymbol{d}}_{\boldsymbol{3}}(\boldsymbol{u}(\boldsymbol{n}) - \boldsymbol{u}(\boldsymbol{n}+\boldsymbol{a}_{\boldsymbol{2}}-\boldsymbol{a}_{\boldsymbol{1}}) + K\ \hat{\boldsymbol{d}}_{\boldsymbol{3}} \otimes \hat{\boldsymbol{d}}_{\boldsymbol{3}}(\boldsymbol{u}(\boldsymbol{n}) - \boldsymbol{u}(\boldsymbol{n}-\boldsymbol{a}_{\boldsymbol{2}}+\boldsymbol{a}_{\boldsymbol{1}}) \\
&\quad + k_b\ \hat{\boldsymbol{d}}_{\boldsymbol{1}} \otimes \hat{\boldsymbol{d}}_{\boldsymbol{1}}(\boldsymbol{u}(\boldsymbol{n}) - \boldsymbol{h}(\boldsymbol{n})) + b\ \hat{\boldsymbol{d}}_{\boldsymbol{1}} \otimes \hat{\boldsymbol{d}}_{\boldsymbol{1}}(\boldsymbol{u}(\boldsymbol{n}) - \boldsymbol{h}(\boldsymbol{n}-\boldsymbol{a}_{\boldsymbol{1}})) \\
&\quad + k_b\ \hat{\boldsymbol{d}}_{\boldsymbol{2}} \otimes \hat{\boldsymbol{d}}_{\boldsymbol{2}}(\boldsymbol{u}(\boldsymbol{n}) - \boldsymbol{r}(\boldsymbol{n})) + b\ \hat{\boldsymbol{d}}_{\boldsymbol{2}} \otimes \hat{\boldsymbol{d}}_{\boldsymbol{2}}(\boldsymbol{u}(\boldsymbol{n}) - \boldsymbol{r}(\boldsymbol{n}-\boldsymbol{a}_{\boldsymbol{2}})) \\
&\quad + k_b\ \hat{\boldsymbol{d}}_{\boldsymbol{3}} \otimes \hat{\boldsymbol{d}}_{\boldsymbol{3}}(\boldsymbol{u}(\boldsymbol{n}) - \boldsymbol{f}(\boldsymbol{n})) + b\ \hat{\boldsymbol{d}}_{\boldsymbol{3}} \otimes \hat{\boldsymbol{d}}_{\boldsymbol{3}}(\boldsymbol{u}(\boldsymbol{n}) - \boldsymbol{f}(\boldsymbol{n}-\boldsymbol{a}_{\boldsymbol{2}}+\boldsymbol{a}_{\boldsymbol{1}}))
\end{aligned} = 0 \tag{S149}$$

$$k_b\ \hat{\boldsymbol{d}}_{\boldsymbol{1}} \otimes \hat{\boldsymbol{d}}_{\boldsymbol{1}}(\boldsymbol{h}(\boldsymbol{n}) - \boldsymbol{u}(\boldsymbol{n})) + b\ \hat{\boldsymbol{d}}_{\boldsymbol{1}} \otimes \hat{\boldsymbol{d}}_{\boldsymbol{1}}(\ddot{\boldsymbol{h}}(\boldsymbol{n}) - \ddot{\boldsymbol{u}}(\boldsymbol{n}+\boldsymbol{a}_{\boldsymbol{1}})) = 0 \tag{S150}$$

$$k_b\ \hat{\boldsymbol{d}}_{\boldsymbol{2}} \otimes \hat{\boldsymbol{d}}_{\boldsymbol{2}}(\boldsymbol{r}(\boldsymbol{n}) - \boldsymbol{u}(\boldsymbol{n})) + b\ \hat{\boldsymbol{d}}_{\boldsymbol{2}} \otimes \hat{\boldsymbol{d}}_{\boldsymbol{2}}(\ddot{\boldsymbol{r}}(\boldsymbol{n}) - \ddot{\boldsymbol{u}}(\boldsymbol{n}+\boldsymbol{a}_{\boldsymbol{2}})) = 0 \tag{S151}$$

$$k_b\ \hat{\boldsymbol{d}}_{\boldsymbol{3}} \otimes \hat{\boldsymbol{d}}_{\boldsymbol{3}}(\boldsymbol{f}(\boldsymbol{n}) - \boldsymbol{u}(\boldsymbol{n})) + b\ \hat{\boldsymbol{d}}_{\boldsymbol{3}} \otimes \hat{\boldsymbol{d}}_{\boldsymbol{3}}(\ddot{\boldsymbol{f}}(\boldsymbol{n}) - \ddot{\boldsymbol{u}}(\boldsymbol{n}-\boldsymbol{a}_{\boldsymbol{2}}+\boldsymbol{a}_{\boldsymbol{1}})) = 0 \tag{S152}$$

From Eqns. (S145), (S146), (S147), (S149), (S150), (S151) and (S152),

$$\begin{aligned}
&M\ddot{u}_x(0,0) + K(u_x - u_x(1,0)) + K(u_x(0,0) - u_x(-1,0)) \\
&\quad + \frac{K}{4}\left(u_x(0,0) - u_x\left(\frac{1}{2},\frac{\sqrt{3}}{2}\right)\right) + \frac{K}{4}\left(u_x(0,0) - u_x\left(-\frac{1}{2},-\frac{\sqrt{3}}{2}\right)\right) \\
&\quad + \frac{K}{4}\left(u_x(0,0) - u_x\left(-\frac{1}{2},\frac{\sqrt{3}}{2}\right)\right) + \frac{K}{4}\left(u_x(0,0) - u_x\left(\frac{1}{2},-\frac{\sqrt{3}}{2}\right)\right) \\
&+ \frac{\sqrt{3}K}{4}\left(u_y(0,0) - u_y\left(\frac{1}{2},\frac{\sqrt{3}}{2}\right)\right) + \frac{\sqrt{3}K}{4}\left(u_y(0,0) - u_y\left(-\frac{1}{2},-\frac{\sqrt{3}}{2}\right)\right) \\
&- \frac{\sqrt{3}K}{4}\left(u_y(0,0) - u_y\left(-\frac{1}{2},\frac{\sqrt{3}}{2}\right)\right) - \frac{\sqrt{3}K}{4}\left(u_y(0,0) - u_y\left(\frac{1}{2},-\frac{\sqrt{3}}{2}\right)\right) \\
&\quad + k_b(u_x(0,0) - h_x(0,0)) + b(\ddot{u}_x(0,0) - \ddot{h}_x(-1,0)) \\
&\quad + \frac{k_b}{4}(u_x(0,0) - r_x(0,0)) + \frac{b}{4}\left(\ddot{u}_x(0,0) - \ddot{r}_x\left(-\frac{1}{2},-\frac{\sqrt{3}}{2}\right)\right) \\
&+ \frac{\sqrt{3}k_b}{4}(u_y(0,0) - r_y(0,0)) + \frac{\sqrt{3}b}{4}\left(\ddot{u}_y(0,0) - \ddot{r}_y\left(-\frac{1}{2},-\frac{\sqrt{3}}{2}\right)\right) \\
&\quad + \frac{k_b}{4}(u_x(0,0) - f_x(0,0)) + \frac{b}{4}\left(\ddot{u}_x(0,0) - \ddot{f}_x\left(\frac{1}{2},-\frac{\sqrt{3}}{2}\right)\right) \\
&- \frac{\sqrt{3}k_b}{4}(u_y(0,0) - f_y(0,0)) - \frac{\sqrt{3}b}{4}\left(\ddot{u}_y(0,0) - \ddot{f}_y\left(\frac{1}{2},-\frac{\sqrt{3}}{2}\right)\right)
\end{aligned} = 0 \tag{S153}$$

$$
\begin{aligned}
&M\ddot{u}_y(0,0)\\
&+\frac{\sqrt{3}K}{4}\left(u_x(0,0)-u_x\left(\frac{1}{2},\frac{\sqrt{3}}{2}\right)\right)+\frac{\sqrt{3}K}{4}\left(u_x(0,0)-u_x\left(-\frac{1}{2},-\frac{\sqrt{3}}{2}\right)\right)\\
&-\frac{\sqrt{3}K}{4}\left(u_y(0,0)-u_y\left(-\frac{1}{2},\frac{\sqrt{3}}{2}\right)\right)-\frac{\sqrt{3}K}{4}\left(u_y(0,0)-u_y\left(\frac{1}{2},-\frac{\sqrt{3}}{2}\right)\right)\\
&-\frac{\sqrt{3}K}{4}\left(u_x(0,0)-u_x\left(-\frac{1}{2},\frac{\sqrt{3}}{2}\right)\right)-\frac{\sqrt{3}K}{4}\left(u_x(0,0)-u_x\left(\frac{1}{2},-\frac{\sqrt{3}}{2}\right)\right)\\
&+\frac{3K}{4}\left(u_y(0,0)-u_y\left(\frac{1}{2},\frac{\sqrt{3}}{2}\right)\right)+\frac{3K}{4}\left(u_y(0,0)-u_y\left(-\frac{1}{2},-\frac{\sqrt{3}}{2}\right)\right)=0
\end{aligned}
\tag{S154}
$$

$$
\begin{aligned}
&+\frac{\sqrt{3}k_b}{4}(u_x(0,0)-r_x(0,0))+\frac{\sqrt{3}b}{4}\left(\ddot{u}_x(0,0)-\ddot{r}_x\left(-\frac{1}{2},-\frac{\sqrt{3}}{2}\right)\right)\\
&+\frac{3k_b}{4}(u_y(0,0)-r_y(0,0))+\frac{3b}{4}\left(\ddot{u}_y(0,0)-\ddot{r}_y\left(-\frac{1}{2},-\frac{\sqrt{3}}{2}\right)\right)\\
&-\frac{\sqrt{3}k_b}{4}(u_x(0,0)-f_x(0,0))-\frac{\sqrt{3}b}{4}\left(\ddot{u}_x-\ddot{f}_x\left(\frac{1}{2},-\frac{\sqrt{3}}{2}\right)\right)\\
&+\frac{3k_b}{4}(u_y(0,0)-f_y(0,0))+\frac{3b}{4}\left(\ddot{u}_y(0,0)-\ddot{f}_y\left(\frac{1}{2},-\frac{\sqrt{3}}{2}\right)\right)
\end{aligned}
$$

$$
k_b(h_x(0,0)-u_x(0,0))+b(\ddot{h}_x(0,0)-\ddot{u}_x(1,0))=0 \tag{S155}
$$

$$
\begin{aligned}
&\frac{k_b}{4}(r_x(0,0)-u_x(0,0))+\frac{b}{4}\left(\ddot{r}_x(0,0)-\ddot{u}_x\left(\frac{1}{2},\frac{\sqrt{3}}{2}\right)\right)\\
&+\frac{\sqrt{3}k_b}{4}(r_y(0,0)-u_y(0,0))+\frac{\sqrt{3}b}{4}\left(\ddot{r}_y(0,0)-\ddot{u}_y\left(\frac{1}{2},\frac{\sqrt{3}}{2}\right)\right)=0
\end{aligned}
\tag{S156}
$$

$$
\begin{aligned}
&\frac{\sqrt{3}k_b}{4}(r_x(0,0)-u_x(0,0))+\frac{\sqrt{3}b}{4}\left(\ddot{r}_x(0,0)-\ddot{u}_x\left(\frac{1}{2},\frac{\sqrt{3}}{2}\right)\right)\\
&+\frac{3k_b}{4}(r_y(0,0)-u_y(0,0))+\frac{3b}{4}\left(\ddot{r}_y(0,0)-\ddot{u}_y\left(\frac{1}{2},\frac{\sqrt{3}}{2}\right)\right)=0
\end{aligned}
\tag{S157}
$$

$$
\begin{aligned}
&\frac{k_b}{4}(f_x(0,0)-u_x(0,0))+\frac{b}{4}\left(\ddot{f}_x(0,0)-\ddot{u}_x\left(-\frac{1}{2},\frac{\sqrt{3}}{2}\right)\right)\\
&-\frac{\sqrt{3}k_b}{4}(f_y(0,0)-u_y(0,0))-\frac{\sqrt{3}b}{4}\left(\ddot{f}_y(0,0)-\ddot{u}_y\left(-\frac{1}{2},\frac{\sqrt{3}}{2}\right)\right)=0
\end{aligned}
\tag{S158}
$$

$$
\begin{aligned}
&-\frac{\sqrt{3}k_b}{4}(f_x(0,0)-u_x(0,0))-\frac{\sqrt{3}b}{4}\left(\ddot{f}_x(0,0)-\ddot{u}_x\left(-\frac{1}{2},\frac{\sqrt{3}}{2}\right)\right)\\
&+\frac{3k_b}{4}(f_y(0,0)-u_y(0,0))+\frac{3b}{4}\left(\ddot{f}_y(0,0)-\ddot{u}_y\left(-\frac{1}{2},\frac{\sqrt{3}}{2}\right)\right)=0
\end{aligned}
\tag{S159}
$$

The components of degrees of freedom in Eqn.(S147) are defined according to the Bloch theorem [5],

$$
u_x(\boldsymbol{n})=U_x e^{n_x a q_x+n_y a q_x+i\omega t} \tag{S160}
$$

$$u_y(\boldsymbol{n}) = U_y e^{n_x a q_x + n_y a q_x + i\omega t} \tag{S161}$$
$$h_x(\boldsymbol{n}) = H_x e^{n_x a q_x + n_y a q_x + i\omega t} \tag{S162}$$
$$r_x(\boldsymbol{n}) = R_x e^{n_x a q_x + n_y a q_x + i\omega t} \tag{S163}$$
$$r_y(\boldsymbol{n}) = R_y e^{n_x a q_x + n_y a q_x + i\omega t} \tag{S164}$$
$$f_x(\boldsymbol{n}) = F_x e^{n_x a q_x + n_y a q_x + i\omega t} \tag{S165}$$
$$f_y(\boldsymbol{n}) = F_y e^{n_x a q_x + n_y a q_y + i\omega t} \tag{S166}$$

where q_x and q_y are wave vectors in the reciprocal space in x and y directions, respectively.

Substituting Eqns. (S160), (S161), (S162), (S163), (S164), (S165) and (S166) into the the equations (S153), (S154), (S155), (S156), (S157), (S158) and (S159), we get

$$-\omega^2[M] + [K] = 0 \tag{S167}$$

where M is mass operator and K is stiffness operator as follows

$$[K] = \begin{bmatrix} \alpha_{1,1} + \frac{3k_b}{2} & \alpha_{1,2} & -k_b & -\frac{k_b}{4} & -\frac{\sqrt{3}k_b}{4} & -\frac{k_b}{4} & \frac{\sqrt{3}k_b}{4} \\ \alpha_{2,1} & \alpha_{2,2} + \frac{3k_b}{2} & 0 & -\frac{\sqrt{3}k_b}{4} & -\frac{3k_b}{4} & \frac{\sqrt{3}k_b}{4} & -\frac{3k_b}{4} \\ -k_b & 0 & k_b & 0 & 0 & 0 & 0 \\ -\frac{k_b}{4} & -\frac{\sqrt{3}k_b}{4} & 0 & \frac{k_b}{4} & \frac{\sqrt{3}k_b}{4} & 0 & 0 \\ -\frac{\sqrt{3}k_b}{4} & -\frac{3k_b}{4} & 0 & \frac{\sqrt{3}k_b}{4} & \frac{3k_b}{4} & 0 & 0 \\ -\frac{k_b}{4} & \frac{\sqrt{3}k_b}{4} & 0 & 0 & 0 & \frac{k_b}{4} & -\frac{\sqrt{3}k_b}{4} \\ \frac{\sqrt{3}k_b}{4} & -\frac{3k_b}{4} & 0 & 0 & 0 & -\frac{\sqrt{3}k_b}{4} & \frac{3k_b}{4} \end{bmatrix} \tag{S168}$$

$$[M] = \begin{bmatrix} M + \frac{3b}{2} & 0 & -be^{-q_x} & -\frac{b}{4}\beta_3 & -\frac{\sqrt{3}b}{4}\beta_3 & -\frac{b}{4}\beta_4 & \frac{\sqrt{3}b}{4}\beta_4 \\ 0 & M + \frac{3b}{2} & 0 & -\frac{\sqrt{3}b}{4}\beta_3 & -\frac{3b}{4}\beta_3 & \frac{\sqrt{3}b}{4}\beta_4 & -\frac{3b}{4}\beta_4 \\ -be^{q_x} & 0 & b & 0 & 0 & 0 & 0 \\ -\frac{b}{4}\beta_1 & -\frac{\sqrt{3}b}{4}\beta_1 & 0 & \frac{b}{4} & \frac{\sqrt{3}b}{4} & 0 & 0 \\ -\frac{\sqrt{3}b}{4}\beta_1 & -\frac{3b}{4}\beta_1 & 0 & \frac{\sqrt{3}b}{4} & \frac{3b}{4} & 0 & 0 \\ -\frac{b}{4}\beta_2 & \frac{\sqrt{3}b}{4}\beta_2 & 0 & 0 & 0 & \frac{b}{4} & -\frac{\sqrt{3}b}{4} \\ \frac{\sqrt{3}b}{4}\beta_2 & -\frac{3b}{4}\beta_2 & 0 & 0 & 0 & -\frac{\sqrt{3}b}{4} & \frac{3b}{4} \end{bmatrix} \tag{S169}$$

where,

$$\begin{aligned} \alpha_{1,1} &= 2K - Ke^{q_x} - Ke^{-q_x} + \frac{K}{4}\left(4 - \beta_1 - \beta_3 - \beta_2 - \beta_4\right) \\ \alpha_{1,2} &= \frac{\sqrt{3}K}{4}(-\beta_1 - \beta_3 + \beta_2 + \beta_4) \\ \alpha_{2,1} &= \frac{\sqrt{3}K}{4}(-\beta_1 - \beta_3 + \beta_2 + \beta_4) \\ \alpha_{2,2} &= \frac{3K}{4}(4 - \beta_1 - \beta_3 - \beta_2 - \beta_4) \\ \beta_1 &= e^{\frac{1}{2}q_x + \frac{\sqrt{3}}{2}q_y} \\ \beta_2 &= e^{-\frac{1}{2}q_x + \frac{\sqrt{3}}{2}q_y} \\ \beta_3 &= e^{-\frac{1}{2}q_x - \frac{\sqrt{3}}{2}q_y} \\ \beta_4 &= e^{\frac{1}{2}q_x - \frac{\sqrt{3}}{2}q_y} \end{aligned} \tag{S170}$$

The degrees of freedom in h_y has been constrained as can be seen. The following matrix operation on both M and K operators will constrain two more degrees of freedoms.

$$\begin{aligned}
K_{C6} &\longrightarrow K_{C_6} - \sqrt{3}K_{C_7} \\
K_{C7} &\longrightarrow 0_{7\times 1} \\
K_{R6} &\longrightarrow K_{R_6} - \sqrt{3}K_{R_7} \\
K_{R7} &\longrightarrow 0_{1\times 7} \\
K_{C4} &\longrightarrow K_{C4} + \sqrt{3}K_{C5} \\
K_{C5} &\longrightarrow 0_{7\times 1} \\
K_{R4} &\longrightarrow K_{R4} + \sqrt{3}K_{R5} \\
K_{R5} &\longrightarrow 0_{1\times 7}
\end{aligned} \tag{S171}$$

$$\begin{aligned}
M_{C6} &\longrightarrow M_{C_6} - \sqrt{3}M_{C_7} \\
M_{C7} &\longrightarrow 0_{7\times 1} \\
M_{R6} &\longrightarrow M_{R_6} - \sqrt{3}M_{R_7} \\
M_{R7} &\longrightarrow 0_{1\times 7} \\
M_{C4} &\longrightarrow M_{C4} + \sqrt{3}M_{C5} \\
M_{C5} &\longrightarrow 0_{7\times 1} \\
M_{R4} &\longrightarrow M_{R4} + \sqrt{3}M_{R5} \\
M_{R5} &\longrightarrow 0_{1\times 7}
\end{aligned} \tag{S172}$$

This will result in a 5×5 M and K operators. Solving for eigenvalue problem will give the results for band structure (shown in Fig. S20 and S21) of triangular lattice.

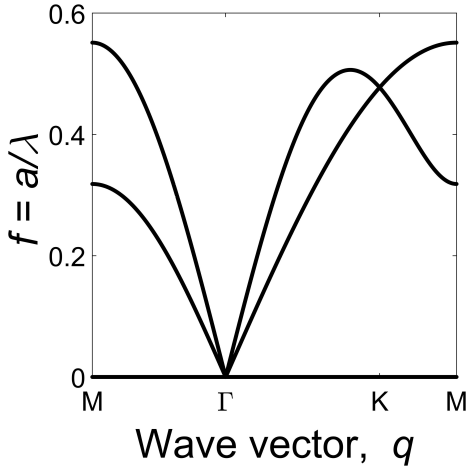

Figure S18: Band structure of inerter-based triangular lattice.

Fig. S18 and Fig. S19 shows the band structure for wave travelling in direction $M-\Gamma-X-M$. Fig. S20 and Fig. S21 shows the band structure in all directions of q_x and q_y.

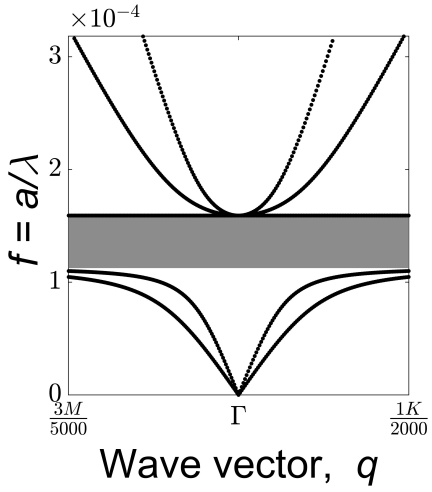

Figure S19: Zoomed version of Fig. S18 showing the band gap.

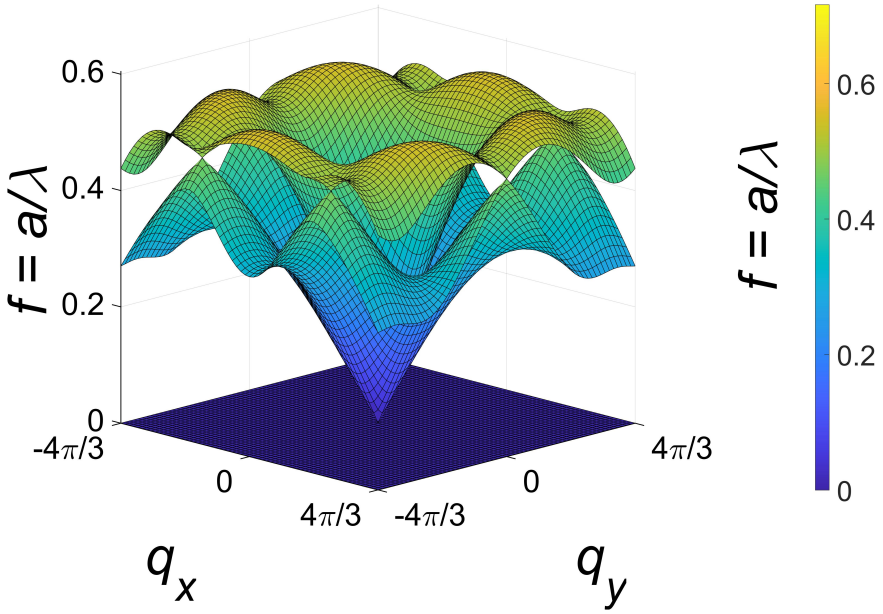

Figure S20: Full band structure for inerter based triangular lattice.

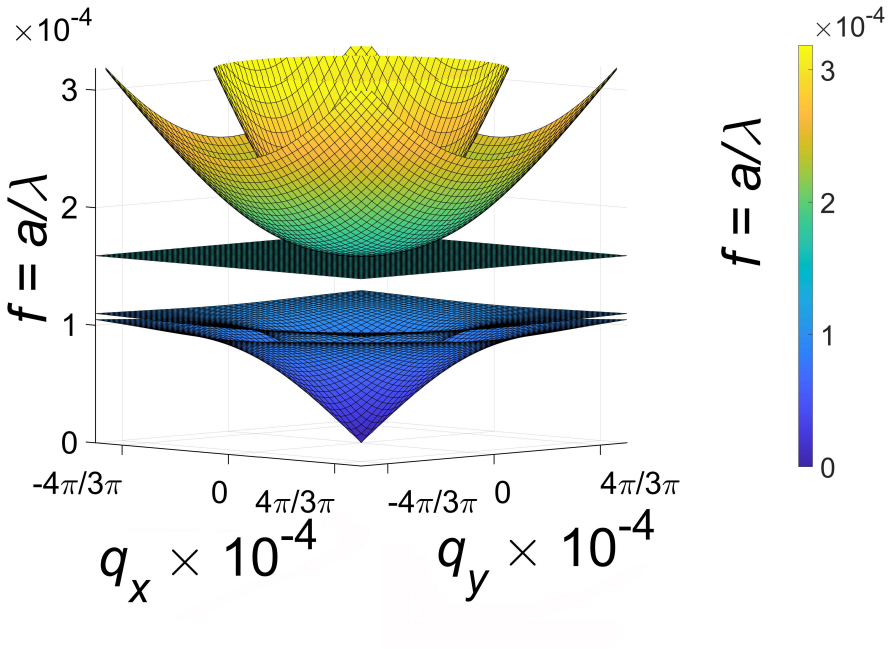

Figure S21: Zoomed band structure for inerter based triangular lattice showing the bandgap.

References

[1] H Al Ba'ba'a, M Nouh, and T Singh. "Formation of local resonance band gaps in finite acoustic metamaterials: A closed-form transfer function model". In: *Journal of Sound and Vibration* 410 (2017), pp. 429–446.

[2] S El-Borgi et al. "Multiple bandgap formation in a locally resonant linear metamaterial beam: Theory and experiments". In: *Journal of Sound and Vibration* 488 (2020), p. 115647.

[3] Michael ZQ Chen et al. "The missing mechanical circuit element". In: *IEEE Circuits and Systems Magazine* 9.1 (2009), pp. 10–26.

[4] Esmaeal Ghavanloo, S Ahmad Fazelzadeh, and Hashem Rafii-Tabar. "Formulation of an efficient continuum mechanics-based model to study wave propagation in one-dimensional diatomic lattices". In: *Mechanics Research Communications* 103 (2020), p. 103467.

[5] Mahmoud I Hussein, Michael J Leamy, and Massimo Ruzzene. "Dynamics of phononic materials and structures: Historical origins, recent progress, and future outlook". In: *Applied Mechanics Reviews* 66.4 (2014).

[6] Yang Liu et al. "Vibration attenuation of finite-size metaconcrete: Mechanism, prediction and verification". In: *Composites Part A: Applied Science and Manufacturing* 143 (2021), p. 106294.

[7] Martin Maldovan and Edwin L Thomas. *Periodic materials and interference lithography: for photonics, phononics and mechanics*. John Wiley & Sons, 2009.

[8] Shigeki Nakaminami et al. "Dynamic testing of a full-scale hydraulic inerter-damper for the seismic protection of civil structures". In: *7th International Conference on Advances in Experimental Structural Engineering, AESE 2017*. Eucentre. 2017, pp. 41–54.

[9] MQ Owaidat. "Determination of the vibrational frequencies of the decorated triangular and centered triangular lattices". In: *The European Physical Journal Plus* 135.2 (2020), pp. 1–13.

[10] Christakis Papageorgiou and Malcolm C Smith. "Laboratory experimental testing of inerters". In: *Proceedings of the 44th IEEE Conference on Decision and Control*. IEEE. 2005, pp. 3351–3356.

[11] Christos Papageorgiou, Neil E Houghton, and Malcolm C Smith. "Experimental testing and analysis of inerter devices". In: *Journal of dynamic systems, measurement, and control* 131.1 (2009).

[12] Kenji Saito and Norio Inoue. "A STUDY ON OPTIMUM RESPONSE CONTROL OF PASSIVE CONTROL SYSTEMS USING VISCOUS DAMPER WITH INERTIAL MASSSubstituting equivalent nonlinear viscous elements for linear viscous elements in optimum control systems". In: *AIJ Journal of Technology and Design* 13.26 (2007).

[13] Yujie Shen et al. "Improved design of dynamic vibration absorber by using the inerter and its application in vehicle suspension". In: *Journal of Sound and Vibration* 361 (2016), pp. 148–158.

[14] Malcolm C Smith. "Synthesis of mechanical networks: the inerter". In: *IEEE Transactions on automatic control* 47.10 (2002), pp. 1648–1662.

[15] Augustus L Stanford and James Mervil Tanner. *Physics for students of science and engineering*. Academic Press, 2014.

[16] XQ Sun et al. "Performance investigation of vehicle suspension system with nonlinear ball-screw inerter". In: *International Journal of Automotive Technology* 17.3 (2016), pp. 399–408.

[17] Fu-Cheng Wang, Min-Feng Hong, and Tz-Chien Lin. "Designing and testing a hydraulic inerter". In: *Proceedings of the Institution of Mechanical Engineers, Part C: Journal of Mechanical Engineering Science* 225.1 (2011), pp. 66–72.

[18] Pai Wang et al. "Harnessing buckling to design tunable locally resonant acoustic metamaterials". In: *Physical review letters* 113.1 (2014), p. 014301.

[19] Ruochen Wang et al. "Design and test of vehicle suspension system with inerters". In: *Proceedings of the Institution of Mechanical Engineers, Part C: Journal of Mechanical Engineering Science* 228.15 (2014), pp. 2684–2689.

[20] Xianchen Xu et al. "Tailoring vibration suppression bands with hierarchical metamaterials containing local resonators". In: *Journal of Sound and Vibration* 442 (2019), pp. 237–248.

[21] Li Yuehao et al. "Modeling, design and experiments of a ball-screw inerter with mechanical diodes". In: *Journal of Sound and Vibration* 504 (2021), p. 116121.

[22] Li Yuehao et al. "Study of dynamic breakdown of inerter and the improved design". In: *Mechanical Systems and Signal Processing* 167 (2022), p. 108520.